

Real-Time Kinematics-Based Sensor-Fault Detection for Autonomous Vehicles Using Single and Double Transport with Adaptive Numerical Differentiation

Shashank Verma^{a,*}, Dennis S. Bernstein^a

^a*Aerospace Department, University of Michigan, 1320 Beal Ave, Ann Arbor, 48109, Michigan, USA*

Abstract

Sensor-fault detection is crucial for the safe operation of autonomous vehicles. This paper introduces a novel kinematics-based approach for detecting and identifying faulty sensors, which is model-independent, rule-free, and applicable to ground and aerial vehicles. This method, called kinematics-based sensor fault detection (KSFD), relies on kinematic relations, sensor measurements, and real-time single and double numerical differentiation. Using onboard data from radar, rate gyros, magnetometers, and accelerometers, KSFD uniquely identifies a single faulty sensor in real time. To achieve this, adaptive input and state estimation (AISE) is used for real-time single and double numerical differentiation of the sensor data, and the single and double transport theorems are used to evaluate the consistency of data. Unlike model-based and knowledge-based methods, KSFD relies solely on sensor signals, kinematic relations, and AISE for real-time numerical differentiation. For ground vehicles, KSFD requires six kinematics-based error metrics, whereas, for aerial vehicles, nine error metrics are used. Simulated and experimental examples are provided to evaluate the effectiveness of KSFD.

Keywords: Kinematics, Sensor fault, Fault detection, Numerical differentiation, Estimation, Adaptive systems, Transport theorem

1. Introduction

Sensor failure can lead to catastrophic outcomes for systems under control, since reliable sensor measurements are critical for proper system functioning. Recent incidents, such as those involving the Boeing 737 Max, attributed to a faulty angle-of-attack sensor, and the tragic crash of Air France Flight 447 on June 1, 2009, caused by a faulty airspeed sensor, highlight the tragic consequences of sensor failure in aircraft.

In autonomous vehicles, various sensors, such as cameras, radar, and LiDAR, are used to perceive the environment. Malfunctioning or failing sensors can result in severe accidents, such as collisions. For instance, a sensor failure might cause an autonomous vehicle to miss a stop sign or traffic light, miscalculate distances or velocities, or fail to detect pedestrians, objects, or other vehicles. As autonomous vehicles become more advanced, they require an increasing number of sensors, which in turn raises the risk of sensor failure. This escalating complexity necessitates advanced methods for detecting and diagnosing sensor faults.

Sensor-fault detection (Samy et al. [1]) is a subset of sensor diagnostics and prognostics (Hwang et al. [2], Doraiswami et al. [3], Isermann [4, 5, 6, 7], Gertler [8], Venkatasubramanian et al. [9], Rengaswamy and Venkatasubramanian [10], Patton and Chen [11], Patton et al. [12], Ding [13], Frank and Ding [14], Chiang et al. [15]). In some cases, sensor health can be assessed by exciting the system in a controlled manner, using a plant model and an observer to predict the response, and by comparing the measured response to the prediction. This approach, known as *active* sensor-fault detection, is based on *residual generation* (Rajamani and Ganguli [16], Frank [17], Chow and Willsky [18], Staroswiecki and Comtet-Varga [19], Isermann [6, 7], Chen and Patton [20], Zhang et al. [21], Freeman

*Corresponding author

Email address: shaaero@umich.edu (Shashank Verma)

et al. [22]). In contrast, *passive* sensor-fault detection detects sensor faults by analyzing each sensor signal separately and searching for anomalies (Martin [23], Kothamasu et al. [24], Yan and Gao [25], Basir and Yuan [26], Basseville [27, 28], Basseville and Nikiforov [29]).

Detecting sensor faults is challenging for several reasons. Sensors can fail gradually, suddenly, or intermittently, with unknown biases, scale factors, and nonlinearities. Additionally, distinguishing sensor failures from the effects of disturbances and system changes can be difficult. The validity of sensor measurements is often most questionable during rare and dangerous events when measurements are most needed to enable corrective action. Therefore, it is essential to detect and diagnose sensor faults promptly to avoid catastrophic events.

Fault detection and isolation methods can be categorized into three categories, namely, hardware redundancy, analytical redundancy, and signal processing (Foullas and Karras [30]). Hardware redundancy methods involve using multiple sensors to provide redundant measurements, increasing the system's complexity and cost (Balaban et al. [31], Blanke et al. [32], Venkatasubramanian et al. [9]).

Analytical redundancy methods, including model-based and knowledge-based approaches, rely on accurate mathematical models or expert knowledge and historical data. These methods are computationally intensive and can struggle with new or unforeseen fault conditions. In autonomous vehicles, machine learning and hybrid approaches have been widely explored. A hybrid method combining the Jarque-Bera test and fuzzy systems is used by (Fang et al. [33]), while (Min et al. [34]) proposes a machine learning-based anomaly detection system. Neural network-based observers for fault detection in autonomous nonlinear systems are presented in (Cao et al. [35]). A deep neural network architecture for multi-sensor-fault detection is discussed in (Safavi et al. [36]). Model-based methods, including the quadratic Kalman filter, are used for UAV fault detection in (Han et al. [37]), whereas (Huang et al. [38]) uses a Luenberger observer for sensor fault detection.

For unmanned aerial vehicles (UAVs), the survey (Foullas and Karras [30], Li et al. [39]) provides an overview of various fault diagnosis and fault-tolerant control methods. Specific approaches, such as sliding mode observers for inertial measurement unit (IMU) sensor fault diagnosis in quadrotor UAVs, are detailed in (Avram et al. [40]). General techniques have been developed for sensor-fault detection across different applications. An online fault detection and diagnosis method combining data-driven and model-based approaches is presented by (Khalastchi et al. [41]). Additionally, a nonlinear fault detection and diagnosis scheme for unmanned quadrotor helicopters is introduced by (Zhong et al. [42]).

Signal-processing-based methods leverage advanced signal analysis techniques for fault detection. For aircraft, (Ansari and Bernstein [43]) presents a sensor fault detection method involving state and input estimation using nonlinear kinematics state space models, while (Ansari and Bernstein [44]) focuses on estimating angular velocity and rate-gyro noise. (Balaban et al. [31]) examines the physical underpinnings of sensor faults and provides insights into fault accommodation strategies. Fault detection in aircraft using kinematic relations is explored in (Van Eykeren and Chu [45, 46]). Additionally, (Fravolini et al. [47]) proposes data-based approaches for robust fault detection of air data sensors.

These studies underscore the importance and diversity of sensor fault detection and diagnosis methods, emphasizing the need for robust and reliable techniques to ensure the safety and reliability of autonomous systems. However, these approaches have several disadvantages. Hardware redundancy increases system cost, complexity, and maintenance due to the need for multiple sensors (Balaban et al. [31]). Hardware redundancy also results in higher power consumption, weight, and size, which are critical constraints in applications such as autonomous vehicles and aerospace (Blanke et al. [32]). Additionally, managing multiple sensors complicates sensor fusion algorithms, potentially causing incorrect fault diagnoses (Venkatasubramanian et al. [9]). Furthermore, hardware redundancy may not effectively detect systematic errors that impact all sensors simultaneously, limiting its reliability (Isermann [48]).

Analytical redundancy, which includes model-based and knowledge-based sensor-fault-detection methods, also has several disadvantages. Model-based approaches require accurate mathematical models of the system, which can be difficult to develop and may not capture all real-world complexities, leading to false alarms or missed faults (Isermann [48]). These methods are computationally intensive and can be challenging to implement in real-time applications with limited processing power. Knowledge-based methods rely heavily on expert knowledge and historical data, which may not always be available or comprehensive (Venkatasubramanian et al. [9]). Furthermore, these methods can struggle with new or unforeseen fault conditions that were not considered during the development phase, limiting their adaptability and robustness (Blanke et al. [32]). Both approaches can also suffer from high implementation and maintenance costs, as they require continuous updates and validation to remain effective (Isermann [48]).

The contribution of this paper is the development and demonstration, both numerically and experimentally, of a novel, real-time-implementable, kinematics-based sensor fault detection (KSFD) approach. KSFD, classified as a signal processing-based method, detects and uniquely identifies the occurrence of a single faulty sensor. KSFD uses kinematics-based error metrics derived from the single- and double-transport theorems, along with real-time numerical differentiation for sensor fault detection. Real-time single and double numerical differentiation are performed using adaptive input and state estimation (AISE), as developed in (Verma et al. [49, 50]). AISE is chosen for numerical differentiation for KSFD because it estimates the derivative causally in real time using sampled data while adapting to unknown and changing sensor-noise characteristics. AISE facilitates the practical implementation of KSFD.

Unlike model-based and knowledge-based methods, KSFD relies solely on sensor signals, kinematic relations, and AISE for real-time numerical differentiation. The present paper thus represents the first use of single and double transport along with single and double real-time numerical differentiation to detect faulty sensors. The authors are not aware of any other sensor-fault-detection technique that operates under these kinematics-based assumptions.

As developed and demonstrated in the present paper, KSFD detects and identifies the occurrence of a single faulty sensor. In cases where two or more sensors fail simultaneously, KSFD indicates the presence of at least one faulty sensor but does not determine which sensors are faulty. However, the scope of this paper is limited to the case of a single sensor fault.

The contents of this paper are organized as follows. Section 2 presents the single and double transport theorems. Section 3 discusses the use of sensor data within these theorems. Section 4 describes AISE. Section 5 introduces the error metrics for sensor-fault detection and their application to ground and aerial vehicles. Section 6 provides a simulated example of sensor-fault detection in an accelerometer. Section 7 presents two experimental examples using real-world data, illustrating KSFD for radar and rate-gyro failures in a ground vehicle. Finally, Section 8 provides an experimental investigation of KSFD for accelerometer failure in an aerial vehicle.

2. Problem Formulation

We assume the Earth is inertially nonrotating and nonaccelerating. The right-handed frame $F_E = [\hat{i}_E \ \hat{j}_E \ \hat{k}_E]$ is fixed to the Earth, and the origin o_E of F_E is any convenient point fixed on the Earth; hence, o_E has zero inertial acceleration. \hat{k}_E points downward, and \hat{i}_E and \hat{j}_E are horizontal. The right-handed vehicle body-fixed frame is denoted by $F_B = [\hat{i}_B \ \hat{j}_B \ \hat{k}_B]$. The origin o_B of F_B is any point fixed on the vehicle, \hat{i}_B is pointing forward of the vehicle, \hat{j}_B is directed out the right side of the vehicle, and \hat{k}_B is directed downward.

Next, F_E and F_B are related by

$$F_B = \vec{R}_{B/E} F_E, \quad (1)$$

where $\vec{R}_{B/E}$ is the physical rotation matrix represented by a 3-2-1 azimuth-elevation-bank Euler rotation sequence involving two intermediate frames $F_{E'}$ and $F_{E''}$. In particular,

$$\vec{R}_{B/E} = \vec{R}_{\hat{i}_{E''}}(\Phi) \vec{R}_{\hat{j}_{E'}}(\Theta) \vec{R}_{\hat{k}_E}(\Psi), \quad (2)$$

where $F_{E'} = \vec{R}_{E'/E} F_E$, $F_{E''} = \vec{R}_{E''/E'} F_{E'}$, the Euler angles $\Psi, \Theta, \Phi \in (-\pi, \pi]$, and the Rodrigues rotation matrix is given by

$$\vec{R}_{\hat{n}}(\kappa) \triangleq (\cos \kappa) \vec{I} + (1 - \cos \kappa) \hat{n} \hat{n}' + (\sin \kappa) \hat{n}^\times, \quad (3)$$

where \vec{I} is the physical identity matrix, and the superscript \times creates a skew-symmetric physical matrix. Note that (3) represents a right-hand-rule rotation about the eigenaxis \hat{n} by the eigenangle κ according to the right-hand rule. The physical angular velocity $\vec{\omega}_{B/E}$ of F_B relative to F_E is defined by Poisson's equation

$$\overset{B\bullet}{\vec{R}}_{B/E} = \vec{R}_{B/E} \overset{\times}{\omega}_{B/E}, \quad (4)$$

where $B\bullet$ denotes the time derivative with respect to F_B .

The location of the vehicle center of mass o_B relative to o_E at each time instant is given by the physical position vector \vec{r}_{o_B/o_E} . The first and second derivatives of \vec{r}_{o_B/o_E} with respect to F_E are given by the single and double transport theorems, respectively, which have the forms

$$\overset{E\bullet}{\vec{r}}_{o_B/o_E} = \overset{B\bullet}{\vec{r}}_{o_B/o_E} + \vec{\omega}_{B/E} \times \vec{r}_{o_B/o_E}, \quad (5)$$

$$\overset{E\bullet\bullet}{\vec{r}}_{o_B/o_E} = \overset{B\bullet\bullet}{\vec{r}}_{o_B/o_E} + 2\vec{\omega}_{B/E} \times \overset{B\bullet}{\vec{r}}_{o_B/o_E} + \overset{B\bullet}{\vec{\omega}}_{B/E} \times \vec{r}_{o_B/o_E} + \vec{\omega}_{B/E} \times (\vec{\omega}_{B/E} \times \vec{r}_{o_B/o_E}). \quad (6)$$

Note that (5) and (6) are exact kinematic relations.

3. Using Sensor Data in Single and Double Transport

The vehicle is equipped with onboard sensors, including magnetometer, radar, rate gyros, and accelerometers. Some radar sensors use the Doppler effect to estimate velocity, in this article we assume that the radar provides only position data. To evaluate the terms in (5) and (6) using sensor data, we begin by resolving all the terms on the right-hand side (RHS) of (5) and (6) in F_B , which yields

$$\begin{bmatrix} r_x \\ r_y \\ r_z \end{bmatrix} \triangleq \vec{r}_{o_B/o_E} \Big|_B, \quad \begin{bmatrix} \dot{r}_x \\ \dot{r}_y \\ \dot{r}_z \end{bmatrix} = \overset{B\bullet}{\vec{r}}_{o_B/o_E} \Big|_B, \quad \begin{bmatrix} \ddot{r}_x \\ \ddot{r}_y \\ \ddot{r}_z \end{bmatrix} = \overset{B\bullet\bullet}{\vec{r}}_{o_B/o_E} \Big|_B, \quad (7)$$

$$\begin{bmatrix} \omega_x \\ \omega_y \\ \omega_z \end{bmatrix} \triangleq \vec{\omega}_{B/E} \Big|_B, \quad \begin{bmatrix} \dot{\omega}_x \\ \dot{\omega}_y \\ \dot{\omega}_z \end{bmatrix} = \overset{B\bullet}{\vec{\omega}}_{B/E} \Big|_B. \quad (8)$$

We resolve (2) in F_B to obtain the orientation (direction cosine) matrix $\mathcal{O}_{E/B}$ given by

$$\begin{aligned} \mathcal{O}_{E/B} &\triangleq \mathcal{O}_{E/B}(\Phi, \Theta, \Psi) \triangleq \vec{R}_{B/E} \Big|_B = \vec{R}_{i_{E'}}(\Phi) \Big|_B \vec{R}_{j_{E'}}(\Theta) \Big|_B \vec{R}_{k_E}(\Psi) \Big|_B \\ &= \begin{bmatrix} (\cos \Theta) \cos \Psi & (\cos \Theta) \sin \Psi & -\sin \Theta \\ (\sin \Phi)(\sin \Theta) \cos \Psi - (\cos \Phi) \sin \Psi & (\sin \Phi)(\sin \Theta) \sin \Psi + (\cos \Phi) \cos \Psi & (\sin \Phi) \cos \Theta \\ (\cos \Phi)(\sin \Theta) \cos \Psi + (\sin \Phi) \sin \Psi & (\cos \Phi)(\sin \Theta) \sin \Psi - (\sin \Phi) \cos \Psi & (\cos \Phi) \cos \Theta \end{bmatrix}^T. \end{aligned} \quad (9)$$

To resolve the left-hand side (LHS) of (5) in F_B , we first resolve the position vector \vec{r}_{o_B/o_E} in F_E to obtain

$$\begin{bmatrix} R_x \\ R_y \\ R_z \end{bmatrix} \triangleq \vec{r}_{o_B/o_E} \Big|_E = \mathcal{O}_{E/B} \begin{bmatrix} r_x \\ r_y \\ r_z \end{bmatrix}, \quad (10)$$

and then we differentiate (10) once and twice to obtain

$$\begin{bmatrix} \dot{R}_x \\ \dot{R}_y \\ \dot{R}_z \end{bmatrix} = \overset{E\bullet}{\vec{r}}_{o_B/o_E} \Big|_E = \frac{d}{dt} \left(\mathcal{O}_{E/B} \begin{bmatrix} r_x \\ r_y \\ r_z \end{bmatrix} \right), \quad (11)$$

$$\begin{bmatrix} \ddot{R}_x \\ \ddot{R}_y \\ \ddot{R}_z \end{bmatrix} = \overset{E\bullet\bullet}{\vec{r}}_{o_B/o_E} \Big|_E = \frac{d^2}{dt^2} \left(\mathcal{O}_{E/B} \begin{bmatrix} r_x \\ r_y \\ r_z \end{bmatrix} \right). \quad (12)$$

Now, define

$$\begin{bmatrix} V_x \\ V_y \\ V_z \end{bmatrix} \triangleq \overset{E\bullet}{\vec{r}}_{o_B/o_E} \Big|_B = \mathcal{O}_{B/E} \begin{bmatrix} \dot{R}_x \\ \dot{R}_y \\ \dot{R}_z \end{bmatrix}, \quad (13)$$

$$\begin{bmatrix} A_x \\ A_y \\ A_z \end{bmatrix} \triangleq \overset{\text{E}\bullet\bullet}{\underset{\text{O}_{\text{B}/\text{O}_{\text{E}}}}{\vec{r}}} \Big|_{\text{B}} = \mathcal{O}_{\text{B}/\text{E}} \begin{bmatrix} \ddot{R}_x \\ \ddot{R}_y \\ \ddot{R}_z \end{bmatrix}, \quad (14)$$

where $\mathcal{O}_{\text{B}/\text{E}} = \mathcal{O}_{\text{E}/\text{B}}^T$. Resolving (5) and (6) in F_{B} , and rewriting (14) yields

$$\begin{bmatrix} V_x \\ V_y \\ V_z \end{bmatrix} = \begin{bmatrix} \dot{r}_x \\ \dot{r}_y \\ \dot{r}_z \end{bmatrix} + \begin{bmatrix} \omega_x \\ \omega_y \\ \omega_z \end{bmatrix} \times \begin{bmatrix} r_x \\ r_y \\ r_z \end{bmatrix}, \quad (15)$$

$$\begin{bmatrix} A_x \\ A_y \\ A_z \end{bmatrix} = \begin{bmatrix} \ddot{r}_x \\ \ddot{r}_y \\ \ddot{r}_z \end{bmatrix} + 2 \begin{bmatrix} \omega_x \\ \omega_y \\ \omega_z \end{bmatrix} \times \begin{bmatrix} \dot{r}_x \\ \dot{r}_y \\ \dot{r}_z \end{bmatrix} + \begin{bmatrix} \dot{\omega}_x \\ \dot{\omega}_y \\ \dot{\omega}_z \end{bmatrix} \times \begin{bmatrix} r_x \\ r_y \\ r_z \end{bmatrix} + \begin{bmatrix} \omega_x \\ \omega_y \\ \omega_z \end{bmatrix} \times \left(\begin{bmatrix} \omega_x \\ \omega_y \\ \omega_z \end{bmatrix} \times \begin{bmatrix} r_x \\ r_y \\ r_z \end{bmatrix} \right), \quad (16)$$

$$\begin{bmatrix} A_x \\ A_y \\ A_z \end{bmatrix} = \mathcal{O}_{\text{B}/\text{E}} \begin{bmatrix} \ddot{R}_x \\ \ddot{R}_y \\ \ddot{R}_z \end{bmatrix}. \quad (17)$$

Furthermore, (15) and (16) are rewritten as

$$\begin{bmatrix} V_x \\ V_y \\ V_z \end{bmatrix} = \begin{bmatrix} \dot{r}_x + (\omega_y r_z - \omega_z r_y) \\ \dot{r}_y + (\omega_z r_x - \omega_x r_z) \\ \dot{r}_z + (\omega_x r_y - \omega_y r_x) \end{bmatrix}, \quad (18)$$

$$\begin{bmatrix} A_x \\ A_y \\ A_z \end{bmatrix} = \begin{bmatrix} \ddot{r}_x + 2(\dot{r}_z \omega_y - \dot{r}_y \omega_z) + (r_z \dot{\omega}_y - r_y \dot{\omega}_z) + \omega_y (r_y \omega_x - r_x \omega_y) + \omega_z (r_z \omega_x - r_x \omega_z) \\ \ddot{r}_y + 2(\dot{r}_x \omega_z - \dot{r}_z \omega_x) + (r_x \dot{\omega}_z - r_z \dot{\omega}_x) + \omega_z (r_z \omega_y - r_y \omega_z) - \omega_x (r_y \omega_x - r_x \omega_y) \\ \ddot{r}_z + 2(\dot{r}_y \omega_x - \dot{r}_x \omega_y) + (r_y \dot{\omega}_x - r_x \dot{\omega}_y) - \omega_x (r_z \omega_x - r_x \omega_z) - \omega_y (r_z \omega_y - r_y \omega_z) \end{bmatrix}. \quad (19)$$

3.1. Ground Vehicles

For ground vehicles, we assume that the azimuth Ψ of the vehicle may vary with time, but otherwise, the vehicle remains horizontal, and thus the elevation Θ and bank Φ angles are identically zero. Table 1 shows the data available from onboard sensors along with the derivatives that are computed to evaluate all of the terms in (15), (16), and (17). To compute these derivatives, we apply AISE described in Section 4. Figure 1 shows the coordinate system for ground-vehicle kinematics. Note that, for ground vehicles, we ignore the z component of the radar and accelerometer data as well as the x and y components of the rate gyro.

Sensors	Data	Processed Data
Radar	r_x, r_y	$\dot{r}_x, \dot{r}_y,$ \ddot{r}_x, \ddot{r}_y
Accelerometer	A_x, A_y	-
Magnetometer	$\mathcal{O}_{\text{B}/\text{E}}(0, 0, \Psi)$	-
Rate gyro	ω_z	$\dot{\omega}_z$

Table 1: On-board sensors for ground vehicles. These sensors, along with numerical differentiation, provide the data needed to evaluate all of the terms in (15), (16), and (17).

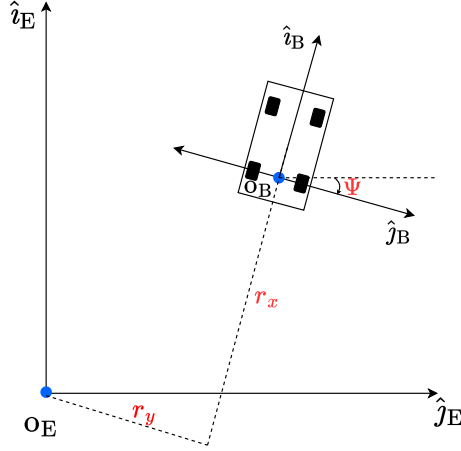


Figure 1: Coordinate frames for the vehicle kinematics under the assumption that the vehicle remains horizontal. \hat{i}_E points north, while \hat{j}_E points east. The vectors \hat{k}_E and \hat{k}_B point vertically downward. r_x, r_y , and Ψ are radar and magnetometer measurements, respectively, as summarized in Table 1.

3.2. Aerial Vehicles

For aerial vehicles, the 3-2-1 Euler angles Ψ , Θ , and Φ represent azimuth, elevation, and bank, respectively. In addition, the components ω_x , ω_y , and ω_z of the angular velocity vector $\vec{\omega}_{B/E}$ resolved in F_B as defined in (8) are the roll rate, pitch rate, and yaw rate, respectively. Table 2 lists the data available from onboard sensors as well as the computed derivatives needed to evaluate all of the terms in (15), (16), and (17). These derivatives are computed using AISE given in Section 4.

Sensors	Data	Processed Data
Radar	r_x, r_y, r_z	$\dot{r}_x, \dot{r}_y, \dot{r}_z,$ $\ddot{r}_x, \ddot{r}_y, \ddot{r}_z$
Accelerometer	A_x, A_y, A_z	-
IMU	$\mathcal{O}_{B/E}(\Phi, \Theta, \Psi)$	-
Rate gyro	$\omega_x, \omega_y, \omega_z$	$\dot{\omega}_x, \dot{\omega}_y, \dot{\omega}_z$

Table 2: On-board sensors for aerial vehicles. These sensors, along with numerical differentiation, provide the data needed to evaluate all of the terms in (15), (16), and (17).

4. Adaptive Input and State Estimation

We summarize AISE (Verma et al. [49, 50, 51]) as it is applied to real-time numerical differentiation for computing the processed data listed in Table 1 and Table 2.

Consider the linear discrete-time SISO system

$$x_{k+1} = Ax_k + Bd_k, \quad (20)$$

$$y_k = Cx_k + D_{2,k}v_k, \quad (21)$$

where $k \geq 0$ is the step, $x_k \in \mathbb{R}^n$ is the unknown state, $d_k \in \mathbb{R}$ is unknown input, $y_k \in \mathbb{R}$ is a measured output, $v_k \in \mathbb{R}$ is standard white noise, and $D_{2,k}v_k \in \mathbb{R}$ is the sensor noise at time $t = kT_s$, where T_s is the sample time. The matrices $A \in \mathbb{R}^{n \times n}$, $B \in \mathbb{R}^{n \times 1}$, and $C \in \mathbb{R}^{1 \times n}$ are assumed to be known, and $D_{2,k}$ is assumed to be unknown. The sensor-noise covariance is $V_{2,k} \triangleq D_{2,k}D_{2,k}^T$. The goal of adaptive input estimation (AIE) is to estimate d_k and x_k .

In the application of AIE to real-time numerical differentiation, we use (20) and (21) to model a discrete-time integrator. As a result, AIE furnishes an estimate denoted by \hat{d}_k for the derivative of the sampled output y_k . For single discrete-time differentiation, $A = 1$, $B = T_s$, and $C = 1$, whereas, for double discrete-time differentiation,

$$A = \begin{bmatrix} 1 & T_s \\ 0 & 1 \end{bmatrix}, \quad B = \begin{bmatrix} \frac{1}{2}T_s^2 \\ T_s \end{bmatrix}, \quad C = [1 \quad 0]. \quad (22)$$

4.1. Input Estimation

AIE comprises three subsystems, namely, the Kalman filter forecast subsystem, the input-estimation subsystem, and the Kalman filter data-assimilation subsystem. First, consider the Kalman filter forecast step

$$x_{fc,k+1} = Ax_{da,k} + B\hat{d}_k, \quad (23)$$

$$y_{fc,k} = Cx_{fc,k}, \quad (24)$$

$$z_k = y_{fc,k} - y_k, \quad (25)$$

where $x_{da,k} \in \mathbb{R}^n$ is the data-assimilation state, $x_{fc,k} \in \mathbb{R}^n$ is the forecast state, \hat{d}_k is the estimate of d_k , $y_{fc,k} \in \mathbb{R}$ is the forecast output, $z_k \in \mathbb{R}$ is the residual, and $x_{fc,0} = 0$.

Next, to obtain \hat{d}_k , the input-estimation subsystem of order n_e is given by the exactly proper, input-output dynamics

$$\hat{d}_k = \sum_{i=1}^{n_e} P_{i,k} \hat{d}_{k-i} + \sum_{i=0}^{n_e} Q_{i,k} z_{k-i}, \quad (26)$$

where $P_{i,k} \in \mathbb{R}$ and $Q_{i,k} \in \mathbb{R}$. AIE minimizes a cost function that depends on z_k by updating $P_{i,k}$ and $Q_{i,k}$ as shown below. The subsystem (26) can be reformulated as

$$\hat{d}_k = \Phi_k \theta_k, \quad (27)$$

where the estimated coefficient vector $\theta_k \in \mathbb{R}^{l_\theta}$ is defined by

$$\theta_k \triangleq [P_{1,k} \quad \cdots \quad P_{n_e,k} \quad Q_{0,k} \quad \cdots \quad Q_{n_e,k}]^T, \quad (28)$$

the regressor matrix $\Phi_k \in \mathbb{R}^{1 \times l_\theta}$ is defined by

$$\Phi_k \triangleq [\hat{d}_{k-1} \quad \cdots \quad \hat{d}_{k-n_e} \quad z_k \quad \cdots \quad z_{k-n_e}], \quad (29)$$

and $l_\theta \triangleq 2n_e + 1$. The subsystem (26) can be written using backward shift operator \mathbf{q}^{-1} as

$$\hat{d}_k = G_{\hat{d}z,k}(\mathbf{q}^{-1})z_k, \quad (30)$$

where

$$G_{\hat{d}z,k} \triangleq D_{\hat{d}z,k}^{-1} N_{\hat{d}z,k}, \quad (31)$$

$$D_{\hat{d}z,k}(\mathbf{q}^{-1}) \triangleq I_{l_d} - P_{1,k}\mathbf{q}^{-1} - \cdots - P_{n_e,k}\mathbf{q}^{-n_e}, \quad (32)$$

$$N_{\hat{d}z,k}(\mathbf{q}^{-1}) \triangleq Q_{0,k} + Q_{1,k}\mathbf{q}^{-1} + \cdots + Q_{n_e,k}\mathbf{q}^{-n_e}. \quad (33)$$

Next, define the filtered signals

$$\Phi_{f,k} \triangleq G_{f,k}(\mathbf{q}^{-1})\Phi_k, \quad \hat{d}_{f,k} \triangleq G_{f,k}(\mathbf{q}^{-1})\hat{d}_k, \quad (34)$$

where, for all $k \geq 0$,

$$G_{f,k}(\mathbf{q}^{-1}) = \sum_{i=1}^{n_f} \mathbf{q}^{-i} H_{i,k}, \quad (35)$$

$$H_{i,k} \triangleq \begin{cases} CB, & k \geq i = 1, \\ C\bar{A}_{k-1} \cdots \bar{A}_{k-(i-1)}B, & k \geq i \geq 2, \\ 0, & i > k, \end{cases} \quad (36)$$

and $\bar{A}_k \triangleq A(I + K_{\text{da},k}C)$, where $K_{\text{da},k}$ is the Kalman filter gain given by (50) below. Furthermore, for all $k \geq 0$, define the *retrospective performance variable* $z_{r,k}: \mathbb{R}^{l_\theta} \rightarrow \mathbb{R}$ by

$$z_{r,k}(\hat{\theta}) \triangleq z_k - (\hat{d}_{f,k} - \Phi_{f,k}\hat{\theta}), \quad (37)$$

and define the *retrospective cost function* $\mathcal{J}_k: \mathbb{R}^{l_\theta} \rightarrow \mathbb{R}$ by

$$\mathcal{J}_k(\hat{\theta}) \triangleq \sum_{i=0}^k \left(\prod_{j=1}^{k-i} \lambda_j \right) [R_z z_{r,i}^2(\hat{\theta}) + R_d (\Phi_i \hat{\theta})^2] + \left(\prod_{j=1}^k \lambda_j \right) (\hat{\theta} - \theta_0)^T R_\theta (\hat{\theta} - \theta_0), \quad (38)$$

where $R_z \in (0, \infty)$, $R_d \in (0, \infty)$, $\lambda_k \in (0, 1]$ is the forgetting factor, and the regularization weighting matrix $R_\theta \in \mathbb{R}^{l_\theta \times l_\theta}$ is positive definite. Then, for all $k \geq 0$, the unique global minimizer

$$\theta_{k+1} \triangleq \arg \min_{\hat{\theta} \in \mathbb{R}^{l_\theta}} \mathcal{J}_k(\hat{\theta}) \quad (39)$$

is given recursively by the RLS update equations (Islam and Bernstein [52], Lai and Bernstein [53])

$$P_{k+1}^{-1} = \lambda_k P_k^{-1} + (1 - \lambda_k) R_\infty + \tilde{\Phi}_k^T \tilde{R} \tilde{\Phi}_k, \quad (40)$$

$$\theta_{k+1} = \theta_k - P_{k+1} \tilde{\Phi}_k^T \tilde{R} (\tilde{z}_k + \tilde{\Phi}_k \theta_k), \quad (41)$$

where $P_0 \triangleq R_\theta^{-1}$, for all $k \geq 0$, $P_k \in \mathbb{R}^{l_\theta \times l_\theta}$ is the positive-definite covariance matrix, the positive-definite matrix $R_\infty \in \mathbb{R}^{l_\theta \times l_\theta}$ is the user-selected *resetting matrix*, and where, for all $k \geq 0$,

$$\tilde{\Phi}_k \triangleq \begin{bmatrix} \Phi_{f,k} \\ \Phi_k \end{bmatrix}, \quad \tilde{z}_k \triangleq \begin{bmatrix} z_k - \hat{d}_{f,k} \\ 0 \end{bmatrix}, \quad \tilde{R} \triangleq \begin{bmatrix} R_z & 0 \\ 0 & R_d \end{bmatrix}.$$

Hence, (40) and (41) recursively update the estimated coefficient vector (28).

The forgetting factor $\lambda_k \in (0, 1]$ in (38) and (40) enables the eigenvalues of P_k to increase, which facilitates adaptation of the input-estimation subsystem (26) (Åström et al. [54]). In addition, the resetting matrix R_∞ in (40) prevents the eigenvalues of P_k from becoming excessively large under conditions of poor excitation (Lai and Bernstein [53]), a phenomenon known as covariance windup (Malik et al. [55]).

Next, variable-rate forgetting based on the F -test (Mohseni and Bernstein [56]) is used to select the forgetting factor $\lambda_k \in (0, 1]$. For all $k \geq 0$, we define the *residual error* at step k by

$$\varepsilon_k \triangleq \tilde{z}_k + \tilde{\Phi}_k \theta_k \in \mathbb{R}^2. \quad (42)$$

The residual error indicates how well the input-estimation subsystem (26) predicts the input one step into the future. Furthermore, for all $k \geq 0$, the sample mean of the residual errors over the previous $\tau \geq 1$ steps is defined by

$$\bar{\varepsilon}_{\tau,k} \triangleq \frac{1}{\tau} \sum_{i=k-\tau+1}^k \varepsilon_i \in \mathbb{R}^2, \quad (43)$$

and the sample variance of the residual errors over the previous τ steps is defined by

$$\Sigma_{\tau,k} \triangleq \frac{1}{\tau} \sum_{i=k-\tau+1}^k (\varepsilon_i - \bar{\varepsilon}_{\tau,k})(\varepsilon_i - \bar{\varepsilon}_{\tau,k})^T \in \mathbb{R}^{2 \times 2}. \quad (44)$$

The approach in (Mohseni and Bernstein [56]) compares $\Sigma_{\tau_n,k}$ to $\Sigma_{\tau_d,k}$, where $\tau_n \geq 1$ is the short-term sample size, and $\tau_d > \tau_n$ is the long-term sample size. If the short-term variance $\Sigma_{\tau_n,k}$ is found to be statistically more

significant than the long-term variance $\Sigma_{\tau_d,k}$, according to the Lawley-Hotelling trace approximation (McKeon [57]), then $\lambda_k < 1$ is chosen to be inversely proportional to its statistical significance. Otherwise, λ_k is set to 1. In particular, for all $k \geq 0$, the forgetting factor is selected as

$$\lambda_k \triangleq \frac{1}{1 + \eta g_k \mathbf{1}[g_k]}, \quad (45)$$

where $\eta \geq 0$ is a tuning parameter, $\mathbf{1}: \mathbb{R} \rightarrow \{0, 1\}$ is the unit step function, and, for all $k \geq 0$,

$$g_k \triangleq \sqrt{\frac{\tau_n}{\tau_d} \frac{\text{tr}(\Sigma_{\tau_n,k} \Sigma_{\tau_d,k}^{-1})}{c}} - \sqrt{F_{2\tau_n,b}^{-1}(1 - \alpha)}, \quad (46)$$

$$a \triangleq \frac{(\tau_n + \tau_d - 3)(\tau_d - 1)}{(\tau_d - 5)(\tau_d - 2)}, \quad (47)$$

$$b \triangleq 4 + \frac{2(\tau_n + 1)}{a - 1}, \quad c \triangleq \frac{2\tau_n(b - 2)}{b(\tau_d - 3)}, \quad (48)$$

and where $\alpha \in [0, 1]$ is the significance level and $F_{2\tau_n,b}^{-1}: [0, 1] \rightarrow \mathbb{R}$ is the inverse cumulative distribution function of the F -distribution with degrees of freedom $2\tau_n$ and b . For further details, see (Mohseni and Bernstein [56]) and (McKeon [57]).

4.2. State Estimation

The forecast variable $x_{\text{fc},k}$ updated by (23) is used to obtain the estimate $x_{\text{da},k}$ of x_k given, for all $k \geq 0$, by the Kalman filter data-assimilation step

$$x_{\text{da},k} = x_{\text{fc},k} + K_{\text{da},k} z_k, \quad (49)$$

where the Kalman filter gain $K_{\text{da},k} \in \mathbb{R}^n$, the data-assimilation error covariance $P_{\text{da},k} \in \mathbb{R}^{n \times n}$, and the forecast error covariance $P_{\text{fc},k+1} \in \mathbb{R}^{n \times n}$ are given by

$$K_{\text{da},k} = -P_{\text{fc},k} C^T (C P_{\text{fc},k} C^T + V_{2,k})^{-1}, \quad (50)$$

$$P_{\text{da},k} = (I_n + K_{\text{da},k} C) P_{\text{fc},k}, \quad (51)$$

$$P_{\text{fc},k+1} = A P_{\text{da},k} A^T + V_{1,k}, \quad (52)$$

where $V_{2,k} \in \mathbb{R}$ is the measurement noise covariance, $V_{1,k}$ is defined by

$$V_{1,k} \triangleq B \text{var}(d_k - \hat{d}_k) B^T + A \text{cov}(x_k - x_{\text{da},k}, d_k - \hat{d}_k) B^T + B \text{cov}(d_k - \hat{d}_k, x_k - x_{\text{da},k}) A^T, \quad (53)$$

and $P_{\text{fc},0} = 0$.

4.3. Adaptive State Estimation

This section summarizes the adaptive state estimation component of AISE. Assuming that, for all $k \geq 0$, $V_{1,k}$ and $V_{2,k}$ are unknown in (52) and (50), the goal is to adapt $V_{1,\text{adapt},k}$ and $V_{2,\text{adapt},k}$ at each step k to estimate $V_{1,k}$ and $V_{2,k}$, respectively. To do this, we define, for all $k \geq 0$, the performance metric $J_k: \mathbb{R}^{n \times n} \times \mathbb{R} \rightarrow \mathbb{R}$ by

$$J_k(V_1, V_2) \triangleq |\hat{S}_k - S_k|, \quad (54)$$

where \hat{S}_k is the sample variance of z_k over $[0, k]$ defined by

$$\hat{S}_k \triangleq \frac{1}{k} \sum_{i=0}^k (z_i - \bar{z}_k)^2, \quad \bar{z}_k \triangleq \frac{1}{k+1} \sum_{i=0}^k z_i, \quad (55)$$

and S_k is the variance of the residual z_k determined by the Kalman filter, given by

$$S_k \triangleq C(AP_{\text{da},k-1}A^T + V_1)C^T + V_2. \quad (56)$$

For all $k \geq 0$, we assume for simplicity that $V_{1,\text{adapt},k} \triangleq \eta_k I_n$, and we define the set \mathcal{S} of minimizers $(\eta_k, V_{2,\text{adapt},k})$ of J_k by

$$\mathcal{S} \triangleq \{(\eta_k, V_{2,\text{adapt},k}) : \eta \in [\eta_L, \eta_U] \text{ and } V_2 \geq 0 \text{ minimize } J_k(\eta I_n, V_2)\}, \quad (57)$$

where $0 \leq \eta_L \leq \eta_U$. Next, defining $J_{f,k} : \mathbb{R} \rightarrow \mathbb{R}$ by

$$J_{f,k}(V_1) \triangleq \widehat{S}_k - C(AP_{\text{da},k-1}A^T + V_1)C^T, \quad (58)$$

and using (56), it follows that (54) can be written as

$$J_k(V_1, V_2) = |J_{f,k}(V_1) - V_2|. \quad (59)$$

We then construct the set $\mathcal{J}_{f,k}$ of positive values of $J_{f,k}$ given by

$$\mathcal{J}_{f,k} \triangleq \{J_{f,k}(\eta I_n) : J_{f,k}(\eta I_n) > 0, \eta_L \leq \eta \leq \eta_U\} \subseteq \mathbb{R}. \quad (60)$$

Following result provides a technique for computing η_k and $V_{2,\text{adapt},k}$ defined in (57).

Proposition 4.1. *Let $k \geq 0$. Then, the following statements hold:*

i) *Assume that $\mathcal{J}_{f,k}$ is nonempty, let $\beta \in [0, 1]$, and define η_k and $V_{2,k}$ by*

$$\eta_k = \arg \min_{\eta \in [\eta_L, \eta_U]} |J_{f,k}(\eta I_n) - \widehat{J}_{f,k}(\beta)|, \quad (61)$$

$$V_{2,\text{adapt},k} = J_{f,k}(\eta_k I_n), \quad (62)$$

where

$$\widehat{J}_{f,k}(\beta) \triangleq \beta \min \mathcal{J}_{f,k} + (1 - \beta) \max \mathcal{J}_{f,k}. \quad (63)$$

Then, $(\eta_k, V_{2,\text{adapt},k}) \in \mathcal{S}$.

ii) *Assume that $\mathcal{J}_{f,k}$ is empty, and define η_k and $V_{2,k}$ by*

$$\eta_k = \arg \min_{\eta \in [\eta_L, \eta_U]} |J_{f,k}(\eta I_n)|, \quad (64)$$

$$V_{2,\text{adapt},k} = 0. \quad (65)$$

Then, $(\eta_k, V_{2,\text{adapt},k}) \in \mathcal{S}$.

Proof: See Section 5.2 of (Verma et al. [49]).

A block diagram of AISE is shown in Figure 2.

5. Sensor-Fault Detection

KSFD computes each term in (17), (18), and (19) using sensor data and derivatives of sensor data. The equation residuals are then used to detect sensor faults. We denote the LHS of (18) by $[L_{s,x,k} \ L_{s,y,k} \ L_{s,z,k}]^T$, the LHS of (19) by $[L_{d,x,k} \ L_{d,y,k} \ L_{d,z,k}]^T$, and the RHS of (17), (18), and (19) by $[R_{a,x,k} \ R_{a,y,k} \ R_{a,z,k}]^T$,

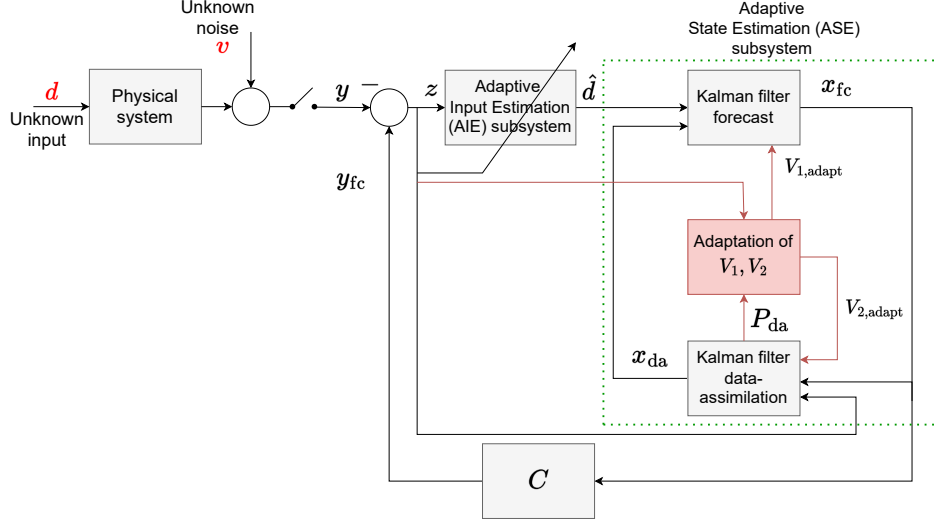


Figure 2: Block diagram of AISE.

$[R_{s,x,k} \ R_{s,y,k} \ R_{s,z,k}]^T$, and $[R_{d,x,k} \ R_{d,y,k} \ R_{d,z,k}]^T$ respectively. Letting $\delta \geq 1$ denote the window size, we define the error metrics for $k > \delta$ by

$$e_{s,q,k} \triangleq \sqrt{\frac{1}{\delta} \sum_{i=k-\delta}^k (L_{s,q,i} - R_{s,q,i})^2}, \quad (66)$$

$$e_{d,q,k} \triangleq \sqrt{\frac{1}{\delta} \sum_{i=k-\delta}^k (L_{d,q,i} - R_{d,q,i})^2}, \quad (67)$$

$$e_{a,q,k} \triangleq \sqrt{\frac{1}{\delta} \sum_{i=k-\delta}^k (L_{d,q,i} - R_{a,q,i})^2}, \quad (68)$$

where q represents x , y , or z . We consider the following types of sensor faults:

- *Bias*: An offset is added to the sensor measurement.
- *Drift*: A ramp is added to the sensor measurement.
- *Sinusoid*: A sinusoid is added to the sensor measurement.
- *Severe noise*: A high level of white noise is added to the sensor measurement.

5.1. Sensor-Fault Detection for Ground Vehicles

Here we apply KSFD to ground vehicles that operate on the horizontal plane. We view the radar as a single sensor providing distance data along the body x and y directions. Under this assumption, there are five relevant sensors, namely, the magnetometer, the radar, the z rate gyro, and the x and y accelerometer. The relevant error metrics are $e_{s,x,k}$, $e_{s,y,k}$, $e_{d,x,k}$, $e_{d,y,k}$, $e_{a,x,k}$, and $e_{a,y,k}$. Table 3 summarizes the sensors used to compute the error metrics (66)–(68) in the case of a ground vehicle which is restricted to horizontal plane.

Error Metric	Sensors
$e_{s,q,k}$	Magnetometer, Radar, Rate gyro
$e_{d,q,k}$	Radar, Rate gyro, Accelerometers
$e_{a,q,k}$	Magnetometer, Radar, Accelerometers

Table 3: Sensors used in KSF D to compute each error metric for the ground vehicle, where q represents x or y .

Each error metric is computed in real time over a trailing data window as the vehicle operates. For each error metric, we specify a cutoff threshold, namely, $c_{s,x}$, $c_{s,y}$, $c_{d,x}$, $c_{d,y}$, $c_{a,x}$, and $c_{a,y}$ for $e_{s,x,k}$, $e_{s,y,k}$, $e_{d,x,k}$, $e_{d,y,k}$, $e_{a,x,k}$, and $e_{a,y,k}$, respectively. At each step k , each error metric is either above cutoff (AC) or below cutoff (BC), and the goal is to use this information to detect faulty sensors. To simplify this procedure, we assume that at most one sensor among the magnetometer, radar, z rate gyro, and x and y accelerometers is faulty at any given time. The method for setting the cutoff thresholds is discussed in the next section.

Considering all possible values of the six error metrics, there are 64 potential scenarios. Assuming that at most one sensor among the magnetometer, radar, z rate gyro, x accelerometer, and y accelerometer is faulty, it follows that, within these 64 cases, only six are feasible. For each of these six cases, Table 4 specifies the cutoff information that identifies the faulty sensor.

$e_{s,x,k}$	$e_{s,y,k}$	$e_{d,x,k}$	$e_{d,y,k}$	$e_{a,x,k}$	$e_{a,y,k}$	Diagnostic
BC	BC	BC	BC	BC	BC	All sensors are healthy
AC	AC	BC	BC	AC	AC	Magnetometer is faulty
AC	AC	AC	AC	AC	AC	Radar is faulty
AC	AC	AC	AC	BC	BC	z Rate gyro is faulty
BC	BC	AC	BC	AC	BC	x Accelerometer is faulty
BC	BC	BC	AC	BC	AC	y Accelerometer is faulty

Table 4: Identification of sensor faults in KSF D for ground vehicles confined to the horizontal plane. At each step, all six error metrics are computed using data obtained during a trailing window. For each metric, BC indicates that the error metric is below cutoff, and AC indicates that the error metric is above cutoff. It is assumed that at most one sensor is faulty; under this assumption, the remaining 58 cases cannot occur.

5.2. Sensor-Fault Detection for Aerial Vehicles

Here we apply KSF D to aerial vehicles. We consider either radar as a single sensor providing distance data along the body x , y , and z directions. We assume that an IMU is responsible for determining the attitude of the vehicle at all times. Under this assumption, there are eight relevant sensors, namely, the IMU, the radar, the x , y , and z rate gyros, and the x , y , and z accelerometers. The relevant error metrics are $e_{s,x,k}$, $e_{s,y,k}$, $e_{s,z,k}$, $e_{d,x,k}$, $e_{d,y,k}$, $e_{d,z,k}$, $e_{a,x,k}$, $e_{a,y,k}$, and $e_{a,z,k}$. Table 5 summarizes the sensors used to compute the error metrics (66)–(68) in the case of an aerial vehicle.

Error Metric	Sensors
$e_{s,q,k}$	IMU, Radar, Rate gyro
$e_{d,q,k}$	Radar, Rate gyro, Accelerometers
$e_{a,q,k}$	IMU, Radar, Accelerometers

Table 5: Sensors used in KSF D to compute each error metric for the aerial vehicle, where q represents x , y , or z .

Similar to Section 5.1, each error metric in KSF D is computed in real time over a trailing data window as the vehicle operates. For each error metric, we specify a cutoff threshold, namely, $c_{s,x}$, $c_{s,y}$, $c_{s,z}$, $c_{d,x}$, $c_{d,y}$, $c_{d,z}$, $c_{a,x}$, $c_{a,y}$, and $c_{a,z}$ for $e_{s,x,k}$, $e_{s,y,k}$, $e_{s,z,k}$, $e_{d,x,k}$, $e_{d,y,k}$, $e_{d,z,k}$, $e_{a,x,k}$, $e_{a,y,k}$, and $e_{a,z,k}$, respectively. At each step k , each error metric is either above cutoff (AC) or below cutoff (BC), and the goal is to use this information to detect faulty sensors. To simplify this procedure, we assume that at most one sensor among the IMU, radar, x , y , and z rate gyros,

and the x , y , and z accelerometer is faulty at any given time. The method for setting the cutoff thresholds is discussed in the next section.

Considering all possible values of the nine error metrics, there are 512 potential scenarios. Assuming that at most one sensor among the IMU, radar, x , y , and z rate gyros, x , y , and z accelerometers is faulty, it follows that, within these 512 cases, only nine are feasible. For each of these nine cases, Table 6 specifies the cutoff information that identifies the faulty sensor.

$e_{s,x,k}$	$e_{s,y,k}$	$e_{s,z,k}$	$e_{d,x,k}$	$e_{d,y,k}$	$e_{d,z,k}$	$e_{a,x,k}$	$e_{a,y,k}$	$e_{a,z,k}$	Diagnostic
BC	All sensors are healthy								
AC	AC	AC	BC	BC	BC	AC	AC	AC	IMU is faulty
AC	Radar is faulty								
AC	AC	BC	AC	AC	AC	BC	BC	BC	z Rate gyro is faulty
AC	BC	AC	AC	AC	AC	BC	BC	BC	y Rate gyro is faulty
BC	AC	AC	AC	AC	AC	BC	BC	BC	x Rate gyro is faulty
BC	BC	BC	BC	BC	AC	BC	BC	AC	z Accelerometer is faulty
BC	BC	BC	BC	AC	BC	BC	AC	BC	y Accelerometer is faulty
BC	BC	BC	AC	BC	BC	AC	BC	BC	x Accelerometer is faulty

Table 6: Identification of sensor faults in KSFDF for aerial vehicles. At each step, all nine error metrics are computed using data obtained during a trailing window. For each error metric, BC indicates that the error metric is below the cutoff, and AC indicates that the error metric is above the cutoff. It is assumed that at most one sensor is faulty; under this assumption, the remaining 503 cases cannot occur.

6. Simulated Application to Ground Vehicle

This section presents a numerical example to illustrate KSFDF on the simulated data. The example addresses sensor fault specifically related to x -axis accelerometer drift. The analysis is confined to cases where motion is restricted to the horizontal (2D) plane. To simulate measurements from the magnetometer, radar, z rate gyro, and x and y accelerometers on a vehicle limited to the horizontal plane, we generate a figure-8 trajectory, as shown in Figure 3.

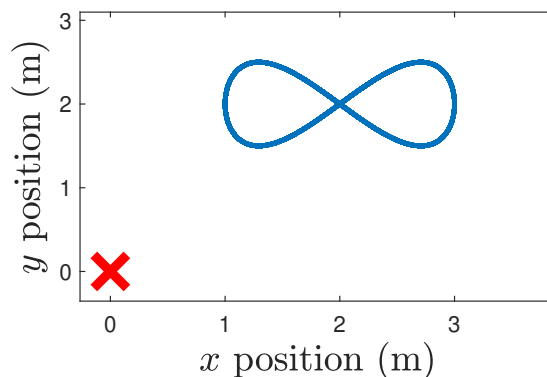


Figure 3: Position trajectory of the vehicle. The red \times has zero inertial acceleration and serves as the radar target. The blue curve represents the simulated trajectory.

The discrete-time equations governing the trajectory are defined by $x(k) = 2 + \sin(2kT_s)$ and $y(k) = 2 + \sin(2kT_s) \cos(2kT_s)$, with the sampling interval $T_s = 0.01$ s/step for $k \in [1, 6000]$. White Gaussian noise is introduced to simulate sensor noise, with standard deviations $\sigma_{r_x} = \sigma_{r_y} = 0.001$ m, $\sigma_{\omega_z} = 0.0001$ rad/s, and $\sigma_{A_x} = \sigma_{A_y} = 0.01g$, where $g = 9.8$ m/s². In Example 6.1, the transient phase for AISE is less than 1000 steps. Therefore, we set $\delta = 1000$ steps. The cutoff thresholds for each error metric are established at twice the rms error due to the sensor noise floor at step $k = 2\delta$. This setting ensures that the computations of the cutoff threshold at step $k = 2\delta$ are not influenced by the transient phase and by the fault starting from step $k = 3\delta$.

Example 6.1. *KSFD for Accelerometer Failure.*

In this scenario, the x -axis accelerometer experiences a failure due to a drift with slope of 0.05 g/s starting at 30 s, where $g = 9.8\text{ m}^2/\text{s}$. For single differentiation using AISE, we set $n_e = 25$, $n_f = 50$, $R_z = 1$, $R_d = 10^{-6.7}$, $R_\theta = 10^{-8}I_{25}$, $\eta = 0.2$, $\tau_n = 5$, $\tau_d = 25$, $\alpha = 0.2$, and $R_\infty = 10^{-4}$. The parameters $V_{1,k}$ and $V_{2,k}$ are adapted, with $\eta_L = 10^{-6}$, $\eta_U = 10^2$, and $\beta = 0.5$ as described in Section 4.3. For double differentiation using AISE, we set $n_e = 20$, $n_f = 18$, $R_z = 1$, $R_d = 10^{-5}$, $R_\theta = 10^{-8}I_{41}$, $\eta = 0.2$, $\tau_n = 5$, $\tau_d = 25$, $\alpha = 0.2$, and $R_\infty = 10^{-7}$. Similarly, $V_{1,k}$ and $V_{2,k}$ are adapted, with $\eta_L = 10^{-6}$, $\eta_U = 10^{-2}$, and $\beta = 0.5$ in Section 4.3.

Figure 4 compares $R_{d,x,k}$ and $R_{d,y,k}$ with their respective $L_{d,x,k}$ and $L_{d,y,k}$. In Figure 5, the drift begins at 30 s and leads to a gradual increase in $e_{d,x,k}$ above the cutoff $c_{d,x}$, which indicates that one of the sensors used to compute $e_{d,x,k}$ is faulty. Figure 6 compares $R_{s,x,k}$ and $R_{s,y,k}$ with $L_{s,x,k}$ and $L_{s,y,k}$. Figure 7 shows that $e_{s,x,k}$ and $e_{s,y,k}$ are below the cutoff threshold. Similarly, Figure 8 and Figure 9 indicates that one of the sensors used to compute $e_{a,x,k}$ is faulty. As observed, $e_{d,x,k}$ and $e_{a,x,k}$ are above the cutoff thresholds, and thus Table 4 implies that the x -axis accelerometer is faulty.

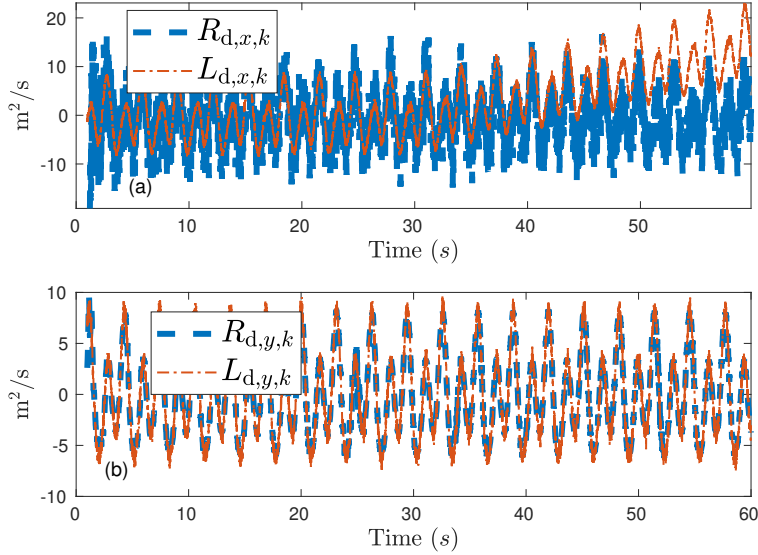


Figure 4: *Example 6.1:* Accelerometer with drift. (a) Beginning at 30 s, $L_{d,x,k}$ exhibits drift. (b) $R_{d,y,k}$ follows $L_{d,y,k}$.

7. Experimental Application to Ground Vehicle

This section provides numerical examples of experimental data to illustrate KSFD in real-world scenarios. This section details the experimental results for a ground vehicle confined to the horizontal plane.

For the experimental setup, an Ackerman car chassis was constructed for the ground vehicle, equipped with a Pixhawk 6C autopilot. The ground rover traced a predefined zig-zag trajectory, set via the ground control application on a tennis court, illustrating the restriction to horizontal (2D) motion as shown in Figure 10a. The sensor data shown in Table 1 were gathered from the Pixhawk 6C logs. Radar sensor faults attributed to high noise as well as x -axis accelerometer faults due to a sinusoid are analyzed in examples 7.1 and 7.2, respectively. For the experimental setup, an Ackerman car chassis was constructed for the ground vehicle, equipped with a Pixhawk 6C autopilot. The ground rover traced a predefined zig-zag trajectory, set via the ground control application on a tennis court, illustrating the restriction to horizontal (2D) motion as shown in Figure 10a. The sensor data shown in Table 1 were gathered from the Pixhawk 6C logs. Radar sensor faults attributed to high noise and x -axis accelerometer faults due to a sinusoid are analyzed in examples 7.1 and 7.2, respectively.

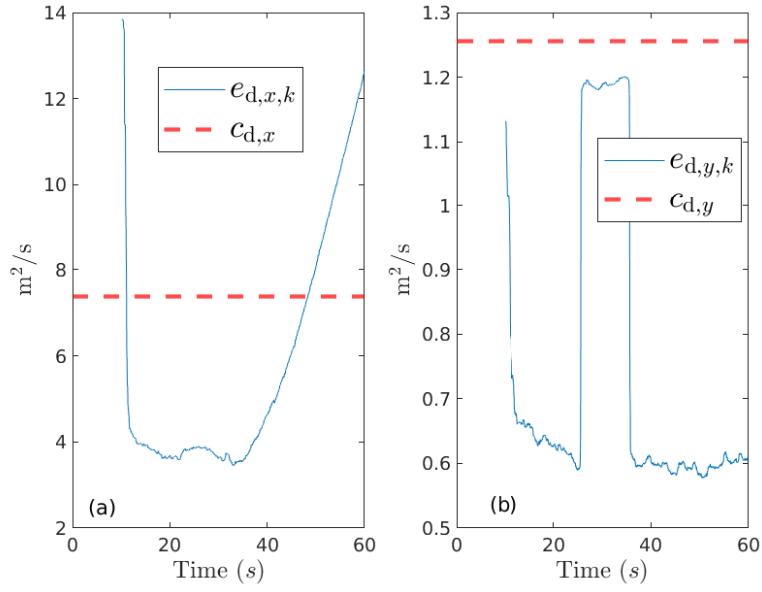


Figure 5: *Example 6.1*: Accelerometer with drift. $e_{d,x,k}$ in (a) gradually increases at 30 s when the drift begins and exceeds the cutoff threshold $c_{d,x}$, which indicates a fault in the sensors used to compute $e_{d,x,k}$. (b) $e_{d,y,k}$ remains below cutoff.

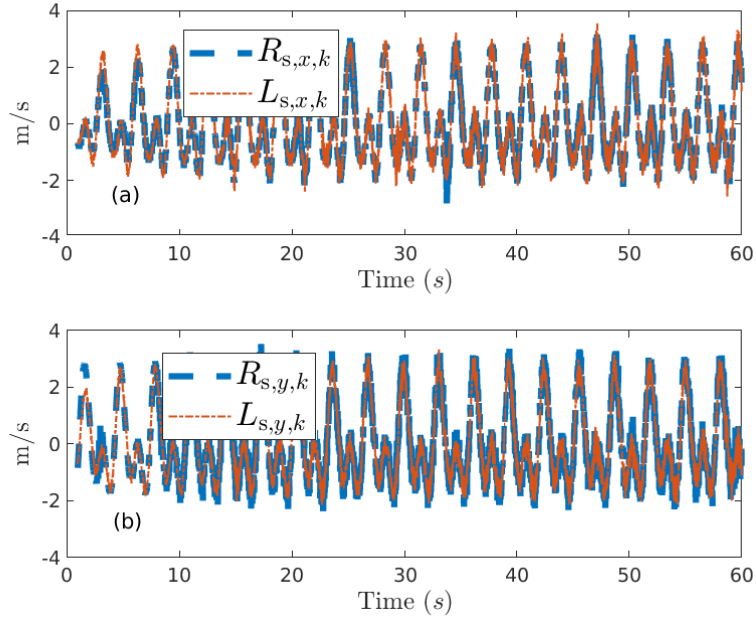


Figure 6: *Example 6.1*: Accelerometer with drift. (a) $R_{s,x,k}$ follows $L_{s,x,k}$. (b) $R_{s,y,k}$ follows $L_{s,y,k}$, which indicates no drift.

In examples 7.1 and 7.2, the transient phase for AISE is concluded within 1000 steps. Consequently, δ is set at 1000 steps. Cutoff thresholds are set at twice the error magnitude at step $k = 1.5\delta$. This parameter choice ensures

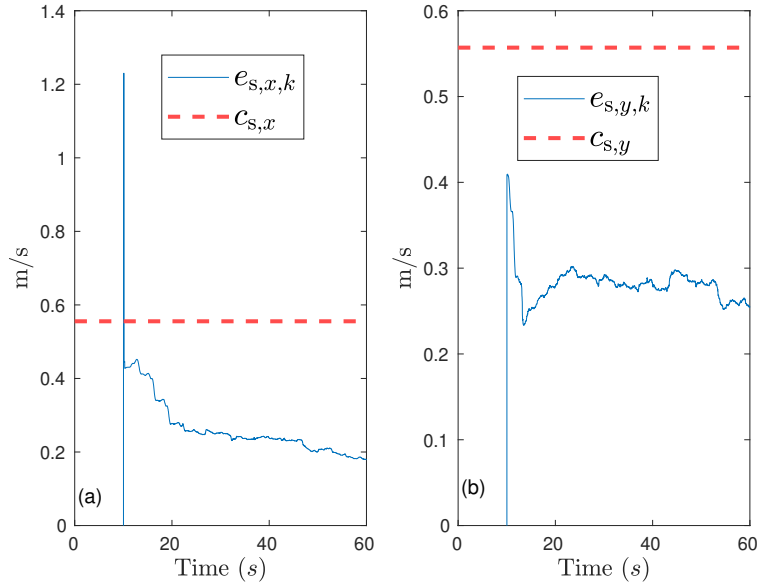


Figure 7: *Example 6.1*: Accelerometer with drift. In (a) and (b), both $e_{s,x,k}$ and $e_{s,y,k}$ remain below the cutoff thresholds $c_{s,x}$ and $c_{s,y}$, respectively, which indicates no sensor fault.

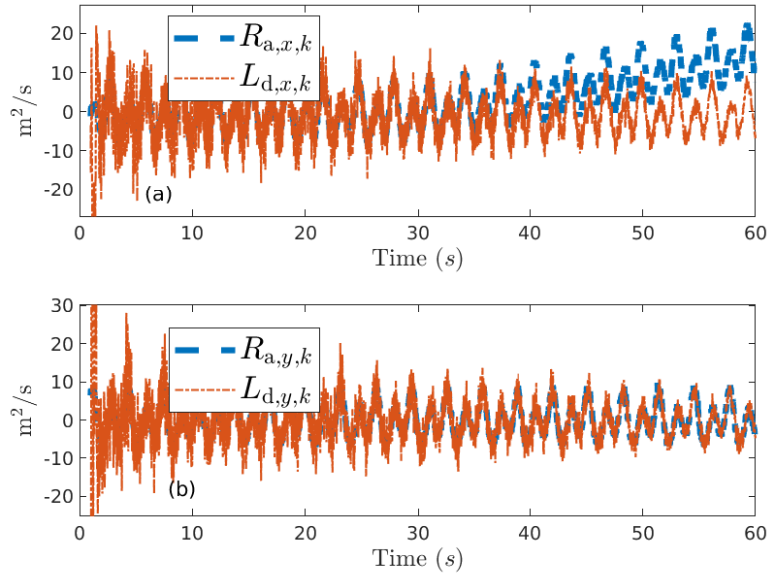


Figure 8: *Example 6.1*: Accelerometer with drift. Beginning at 30 s, $R_{a,x,k}$ in (a) exhibits drift. (b) $R_{a,y,k}$ follows $L_{d,y,k}$.

that the data employed to compute the error metric at step $k = 1.5\delta$ are unaffected by the transient phase and by the fault starting from step $k = 2\delta$.

Example 7.1. KSFDF for Radar failure.

In this scenario, the radar experiences a failure due to high white noise with a standard deviation of 1.0 m,

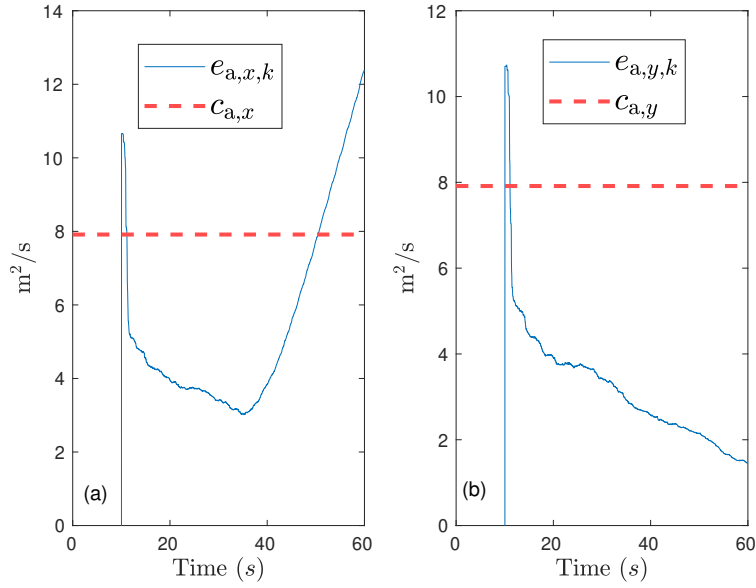


Figure 9: *Example 6.1*: Accelerometer with drift. $e_{a,x,k}$ in (a) gradually increases at 30 s when the drift begins and exceeds the cutoff threshold $c_{a,x}$, which indicates a fault in the sensors used to compute $e_{a,x,k}$. (b) $e_{a,y,k}$ remains below cutoff.

beginning at 20 s. The parameter settings are the same as those used in *Example 6.1*.

Figure 11 compares $R_{d,x,k}$ and $R_{d,y,k}$ with their respective $L_{d,x,k}$ and $L_{d,y,k}$. Figure 12 demonstrates that the onset of high noise at 20 s causes an abrupt increase in $e_{d,x,k}$ and $e_{d,y,k}$, exceeding the cutoff thresholds $c_{d,x}$ and $c_{d,y}$, respectively, which indicates a fault in one of the sensors used to compute $e_{d,x,k}$ and $e_{d,y,k}$. Figure 13 displays comparisons of $R_{s,x,k}$ and $R_{s,y,k}$ with $L_{s,x,k}$ and $L_{s,y,k}$. Likewise, Figure 14 illustrates that the high noise starting at 20 s results in significant increases in $e_{s,x,k}$ and $e_{s,y,k}$ above the cutoffs $c_{s,x}$ and $c_{s,y}$, respectively, signaling faults in the associated sensors. Figures 15 and 16 further indicate sensor faults, as $e_{a,x,k}$ and $e_{a,y,k}$ also exceed their respective cutoff thresholds. Given that all error metrics exceed their cutoff thresholds, Table 4 implies that the radar sensor is faulty.

Example 7.2. KSFDF for rate-gyro failure.

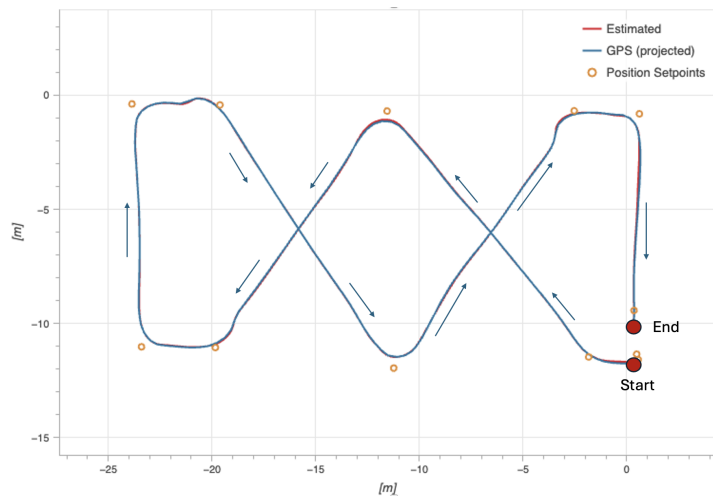
In this scenario, the z -axis rate gyro encounters a failure due to the sinusoidal sensor noise $0.5 \sin(0.1kT_s)$ starting at 30 s. The parameters for both single and double differentiation using AISE are the same as those used in *Example 6.1*, except for $\alpha = 0.05$ for both single and double differentiation.

Figure 17 compares $R_{d,x,k}$ and $R_{d,y,k}$ with their respective $L_{d,x,k}$ and $L_{d,y,k}$. Figure 18 illustrates that the sinusoid fault, commencing at 30 s, results in a sharp increase in $e_{d,x,k}$ and $e_{d,y,k}$ above the cutoff $c_{d,x}$ and $c_{d,y}$, suggesting a fault in one of the sensors contributing to $e_{d,x,k}$ and $e_{d,y,k}$. Figure 19 displays a comparison between $R_{s,x,k}$ and $R_{s,y,k}$, and $L_{s,x,k}$ and $L_{s,y,k}$. Similarly, Figure 20 shows that $e_{s,x,k}$ and $e_{s,y,k}$ go above cutoff thresholds when the sensor fault begins at 30 s. Figures 21 and 22 indicates no sensor fault. Given that $e_{d,x,k}$, $e_{d,y,k}$, $e_{s,x,k}$, and $e_{s,y,k}$ exceed their respective cutoff thresholds, Table 4 implies that the z -axis rate gyro is faulty.

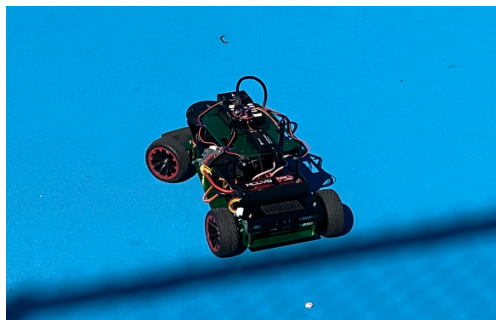
8. Experimental Application to an Aerial Vehicle

This section provides numerical examples of experimental data to illustrate KSFDF in real-world scenarios. This section details the experimental results for a quadcopter in 3D space.

For the experimental setup, a S500 Quadcopter frame was used, equipped with a Pixhawk 4 autopilot. The quadcopter executed a predefined Hilbert curve, as programmed in the ground control application, as shown in Figure



(a)



(b)

Figure 10: (a) Position trajectory of the ground vehicle. (b) Ackerman car chassis ground vehicle used in the experiment.

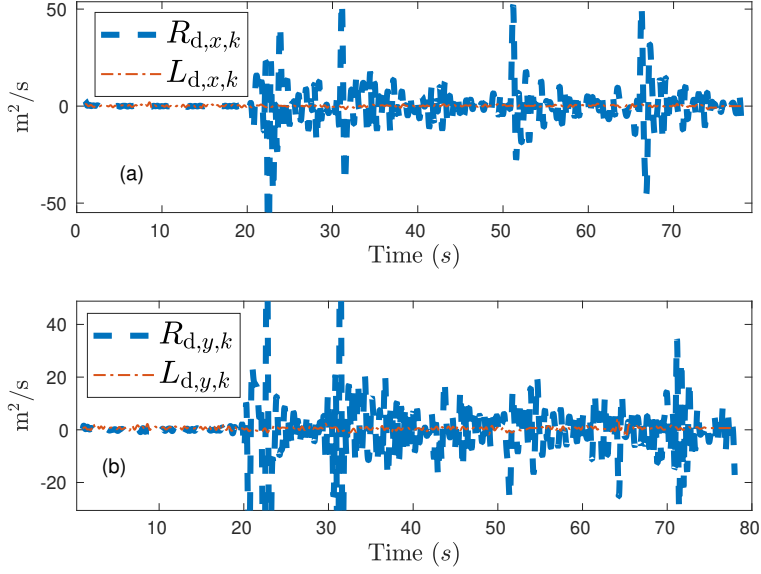


Figure 11: *Example 7.1*: Radar data with high noise. Starting at 20 s, $R_{d,x,k}$ in (a) and $R_{d,y,k}$ in (b) exhibit high noise levels, respectively.

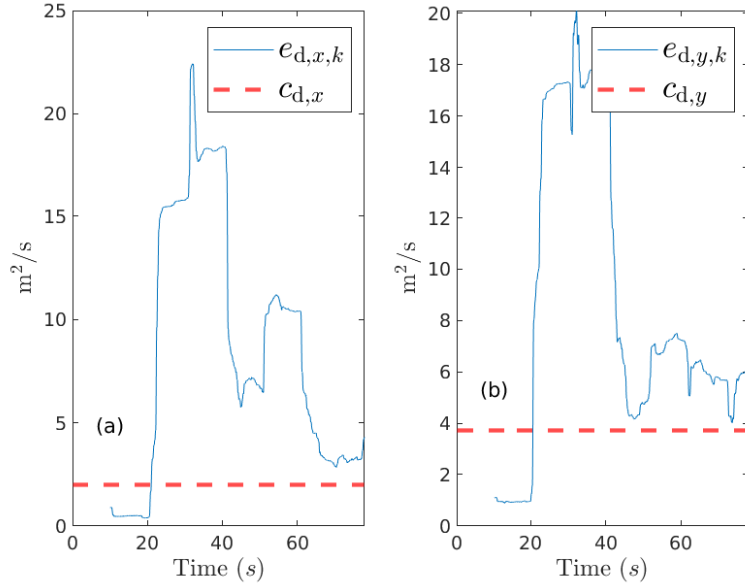


Figure 12: *Example 7.1*: Radar data with high noise. $e_{d,x,k}$ in (a) and $e_{d,y,k}$ in (b) abruptly increase above the cutoff thresholds $c_{d,x}$ and $c_{d,y}$, respectively, at 20 s when the high noise begins, which indicates a fault in the sensors used to compute $e_{d,x,k}$ and $e_{d,y,k}$.

23a. The sensor data displayed in Table 1 were obtained from the Pixhawk 4 logs and via a MOCAP system. A x -axis accelerometer sensor fault due to bias is analyzed in example 8.1.

In example 8.1, the transient phase for AISE is concluded within 1000 steps. Consequently, δ is set at 1000 steps. Cutoff thresholds are set at twice the error magnitude at step $k = 3.5\delta$. This parameter choice ensures that the data

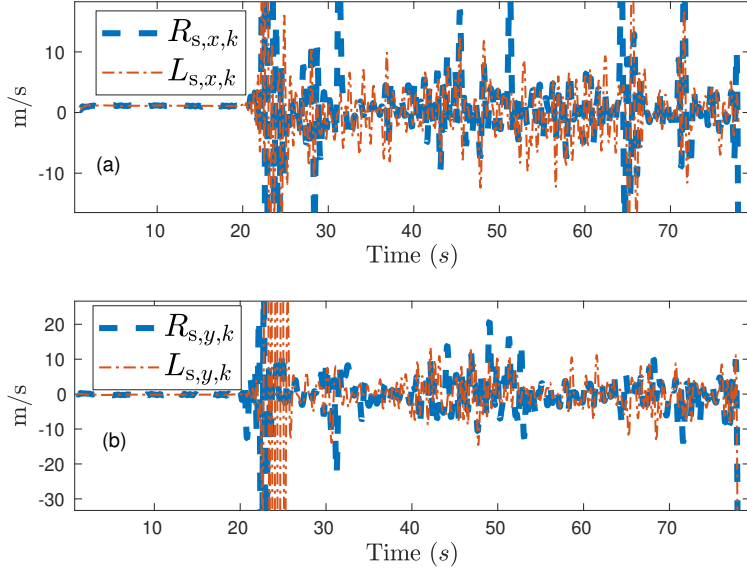


Figure 13: *Example 7.1*: Radar data with high noise. Starting at 20 s, $R_{s,x,k}, L_{s,x,k}$ in (a) and $R_{s,y,k}, L_{s,y,k}$ in (b) exhibit high noise levels, respectively.

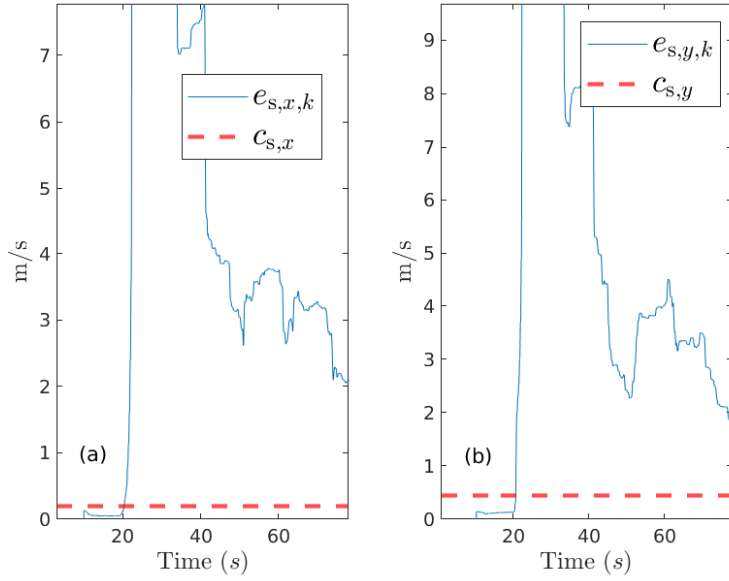


Figure 14: *Example 7.1*: Radar data with high noise. $e_{s,x,k}$ in (a) and $e_{s,y,k}$ in (b) abruptly increase above the cutoff thresholds $c_{s,x}$ and $c_{s,y}$, respectively, at 20 s when the high noise begins, which indicates a fault in the sensors used to compute $e_{s,x,k}$ and $e_{s,y,k}$.

employed to compute the error metric at step $k = 3.5\delta$ are unaffected by the transient phase and by the fault starting from step $k = 4\delta$.

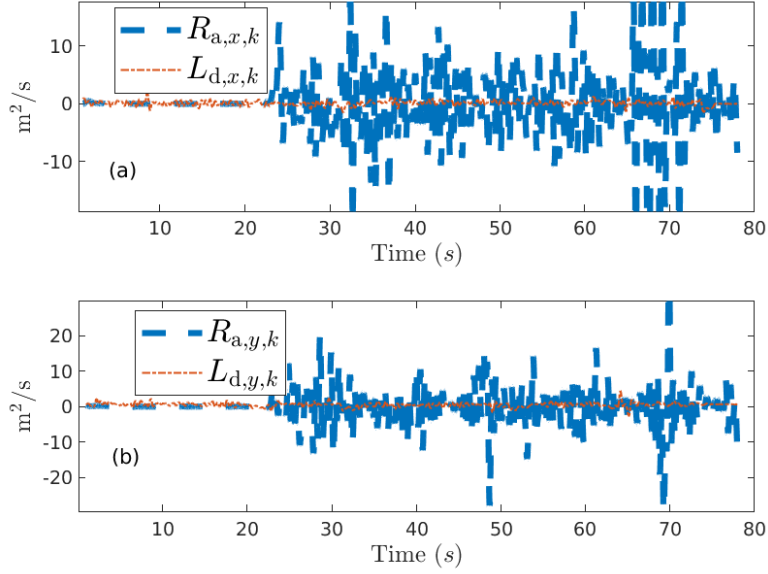


Figure 15: *Example 7.1*: Radar with high noise. Starting at 20 s, $R_{a,x,k}$ in (a) and $R_{a,y,k}$ in (b) exhibit high noise levels, respectively.

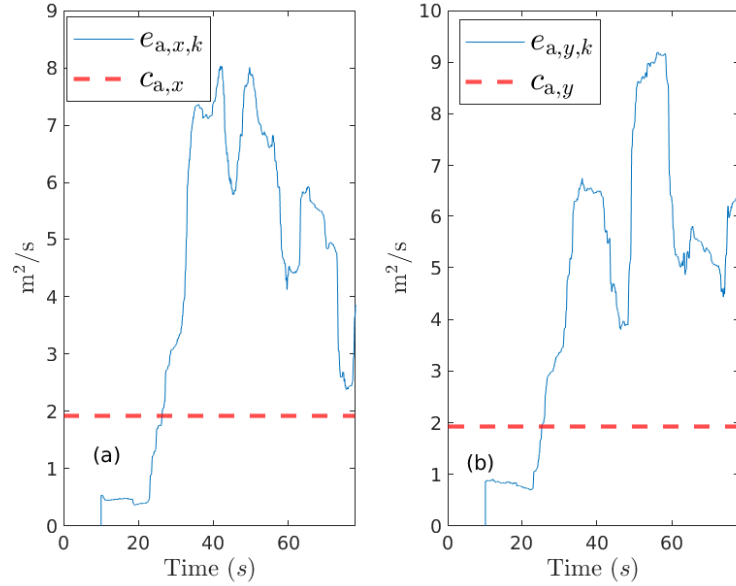


Figure 16: *Example 7.1*: Radar with high noise. $e_{a,x,k}$ in (a) and $e_{a,y,k}$ in (b) abruptly increase above the cutoff thresholds $c_{a,x}$ and $c_{a,y}$, respectively, at 20 s when the high noise begins, which indicates a fault in the sensors used to compute $e_{a,x,k}$ and $e_{a,y,k}$.

Example 8.1. *KSFD for x -axis accelerometer failure.*

In this scenario, the x -axis accelerometer experiences a failure due to a bias of $0.5 g$ starting at 40 s. The parameter settings are the same as those used in Example 6.1.

Figure 24 compares $R_{d,x,k}$, $R_{d,y,k}$, and $R_{d,z,k}$ with their respective $L_{d,x,k}$, $L_{d,y,k}$, and $L_{d,z,k}$. In Figure 25, the

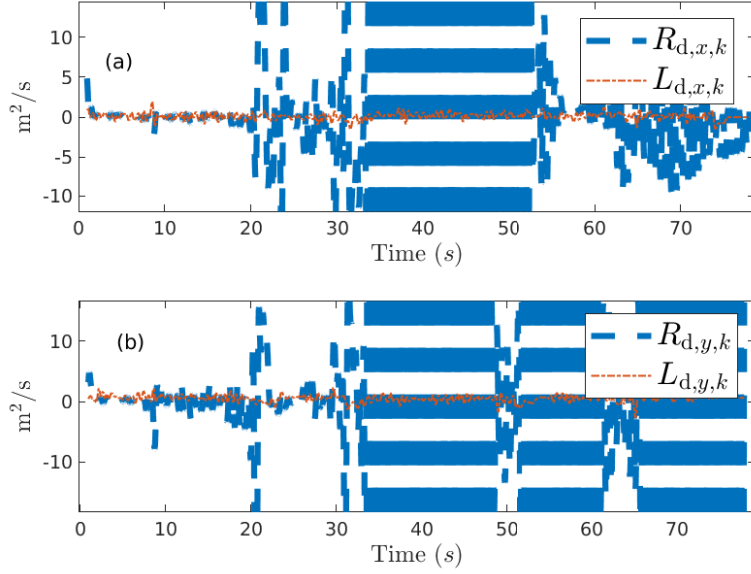


Figure 17: *Example 7.2*: Rate gyro with sinusoid fault. Beginning at 30 s, $R_{d,x,k}$ in (a) and $R_{d,y,k}$ in (b) exhibits sinusoid fault and diverge from $L_{d,x,k}$ and $L_{d,y,k}$, respectively.

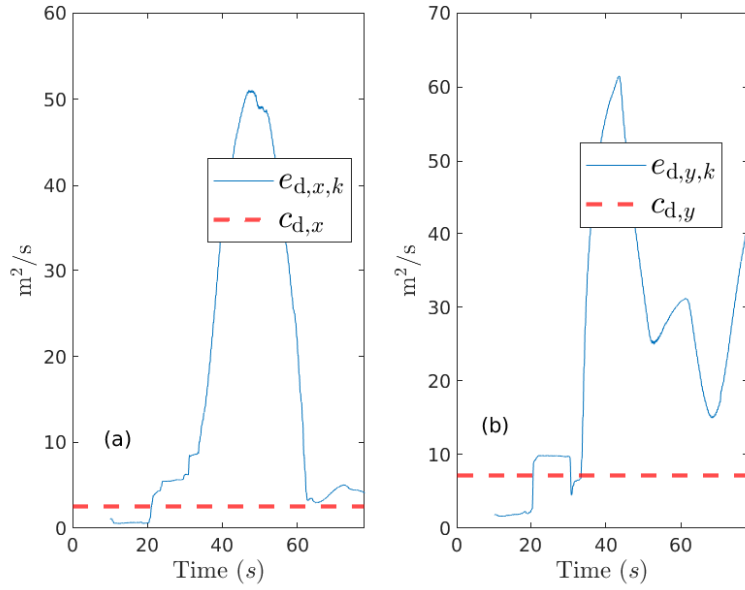


Figure 18: *Example 7.2*: Rate gyro with sinusoid fault. $e_{d,x,k}$ in (a) and $e_{d,y,k}$ in (b) abruptly increase above the cutoff thresholds $c_{d,x}$ and $c_{d,y}$, respectively, at 30 s when the sinusoid fault begins, which indicates a fault in the sensors used to compute $e_{d,x,k}$ and $e_{d,y,k}$.

bias introduced at 40 s leads to a sudden increase in $e_{d,x,k}$ above the cutoff threshold, which indicates that one of the sensors used to compute $e_{d,x,k}$ is faulty. Figure 26 displays a comparison between $R_{s,x,k}$, $R_{s,y,k}$, and $R_{s,z,k}$, with $L_{s,x,k}$, $L_{s,y,k}$, and $L_{s,z,k}$. In contrast, Figure 27 indicates that $e_{s,x,k}$, $e_{s,y,k}$, and $e_{s,z,k}$ remain below the cutoff

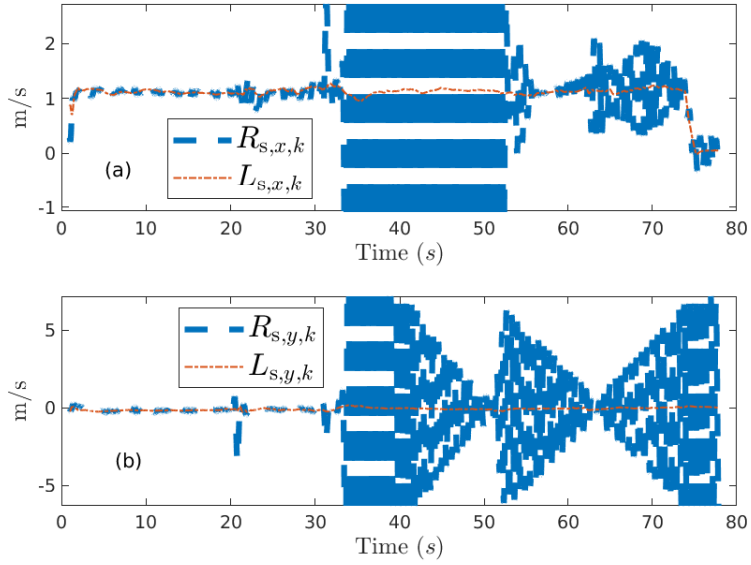


Figure 19: *Example 7.2*: Rate gyro with sinusoid fault. Beginning at 30 s, $R_{s,x,k}$ in (a) and $R_{s,y,k}$ in (b) exhibits sinusoid fault and diverge from $L_{s,x,k}$ and $L_{s,y,k}$, respectively.

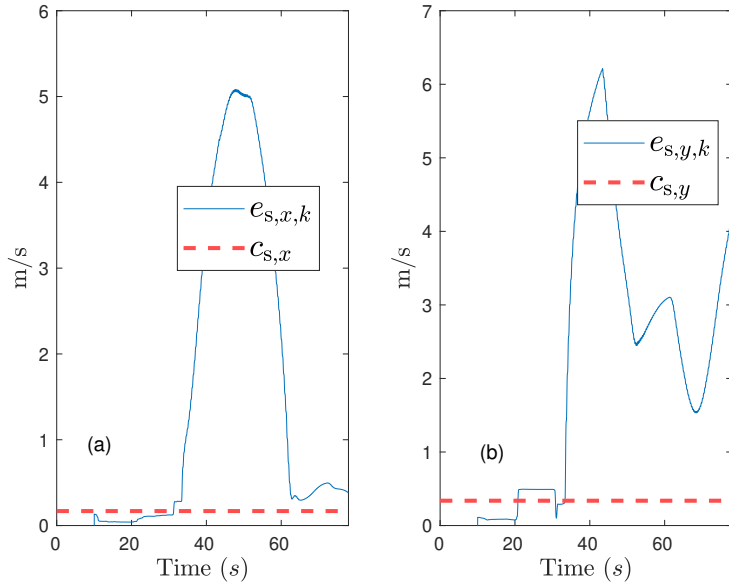


Figure 20: *Example 7.2*: Rate gyro with sinusoid fault. $e_{s,x,k}$ in (a) and $e_{s,y,k}$ in (b) abruptly increase above the cutoff thresholds $c_{s,x}$ and $c_{s,y}$, respectively, at 30 s when the sinusoid fault begins, exceeding cutoff thresholds, which indicates a fault in the sensors used to compute $e_{s,x,k}$ and $e_{s,y,k}$.

threshold. Similarly, Figures 28 and 29 highlight faults in the sensors calculating $e_{a,x,k}$. Given that $e_{d,x,k}$ and $e_{a,x,k}$ exceed their respective cutoff thresholds, Table 4 implies that the x -axis accelerometer is faulty.

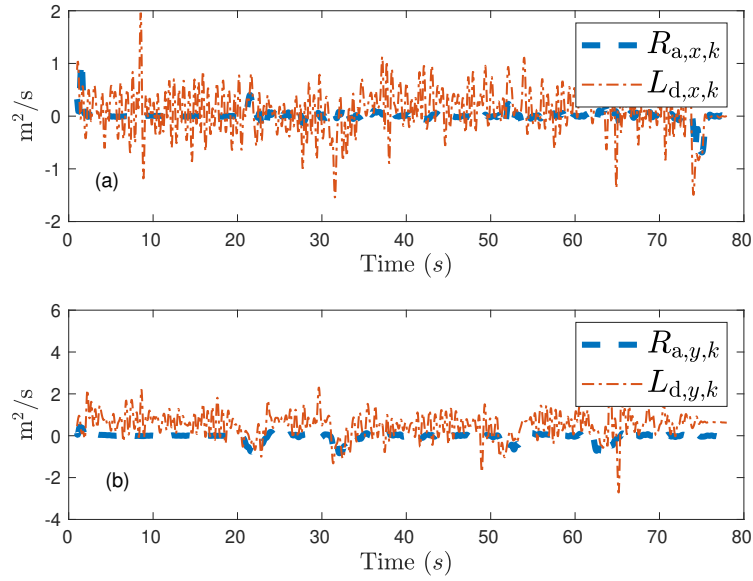


Figure 21: *Example 7.2*: Rate gyro with sinusoid fault. $L_{a,x,k}$ in (a) and $L_{a,y,k}$ in (b) follows $R_{a,x,k}$ and $R_{d,y,k}$, respectively.

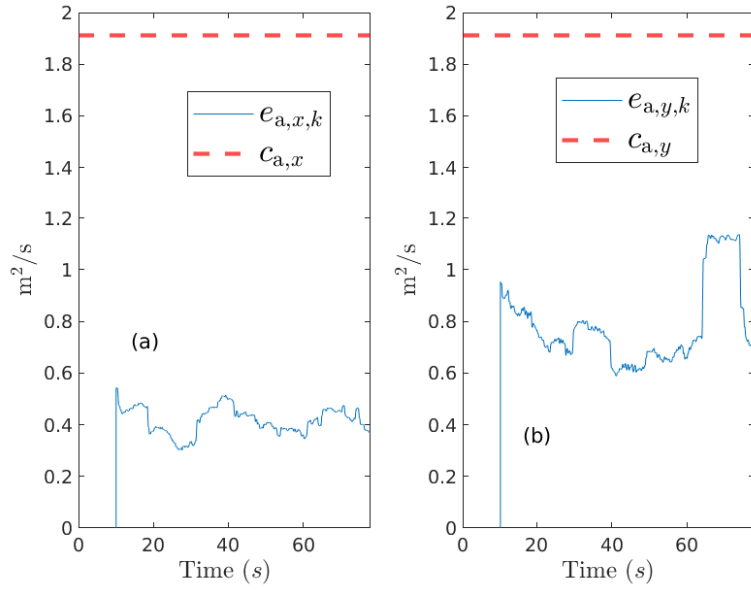
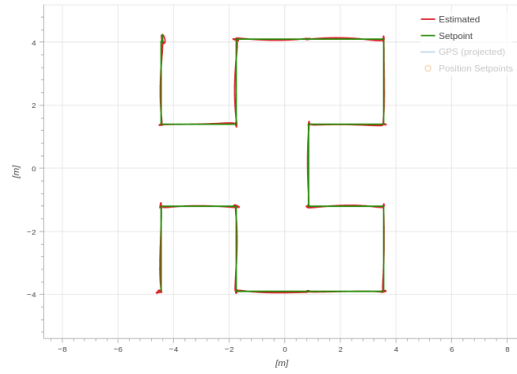


Figure 22: *Example 7.2*: Rate gyro with a sinusoid fault. $e_{a,x,k}$ and $e_{a,y,k}$ remains below cutoff thresholds.

9. Conclusions

This paper introduced kinematics-based sensor fault detection (KSFD) for detecting and identifying faulty sensors in autonomous vehicles. KSFD, which is model-independent, leverages kinematic relations, sensor measurements, and real-time single and double numerical differentiation using the adaptive input and state estimation (AISE). By



(a)



(b)

Figure 23: (a) Position trajectory of the quadcopter shown in $x - y$ plane. (b) Quadcopter vehicle used in the experiment.

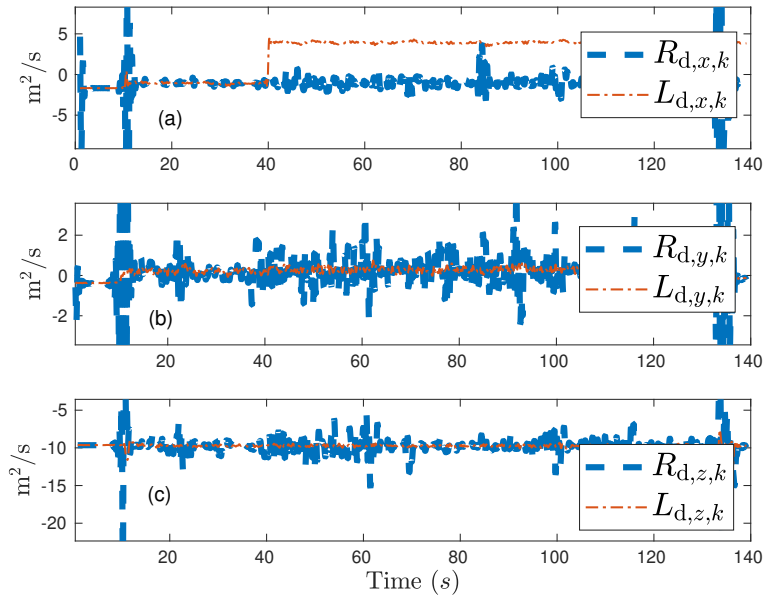


Figure 24: *Example 8.1*: x -axis accelerometer with bias. Beginning at 40 s, $L_{d,x,k}$ in (a) exhibit bias and thus diverge from $R_{d,x,k}$. $R_{d,y,k}$ and $R_{d,z,k}$ follows $L_{d,y,k}$ and $L_{d,z,k}$.

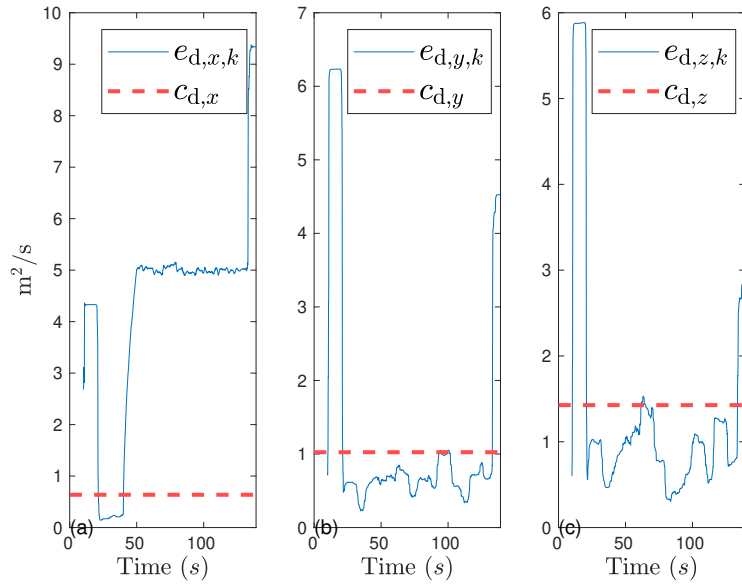


Figure 25: *Example 8.1*: x -axis accelerometer with bias. $e_{d,x,k}$ in (a) abruptly increases above the cutoff threshold $c_{d,x}$ at 40 s when the bias begins, which indicates that one of the sensors used to compute $e_{d,x,k}$ is faulty. $e_{d,y,k}$ and $e_{d,z,k}$ remain below the cutoff thresholds $c_{d,y}$ and $c_{d,z}$.

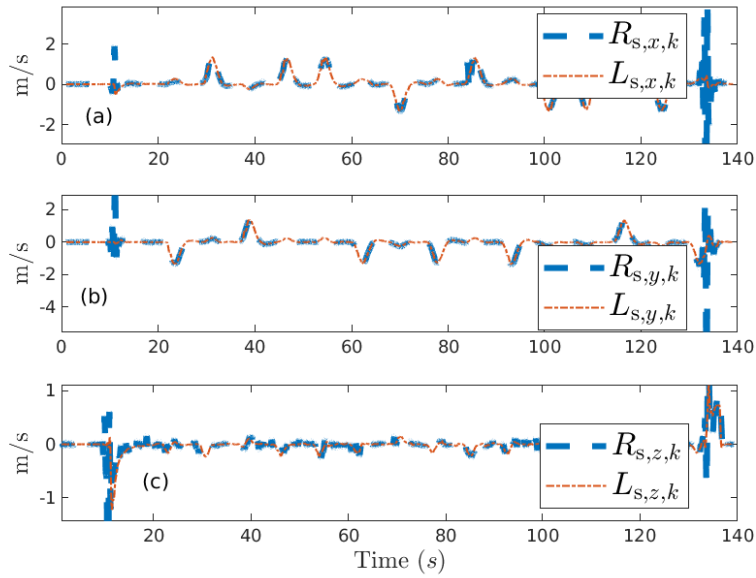


Figure 26: *Example 8.1*: x -axis accelerometer with bias. $R_{s,x,k}$, $R_{s,y,k}$, and $R_{s,z,k}$ follows $L_{d,x,k}$, $L_{d,y,k}$, and $L_{d,z,k}$ in (a), (b), and (c), respectively.

employing kinematics-based error metrics, this approach identifies sensor faults in both ground and aerial vehicles.

For ground vehicles operating in the horizontal plane, KSFD uses six real-time-computed, kinematics-based error

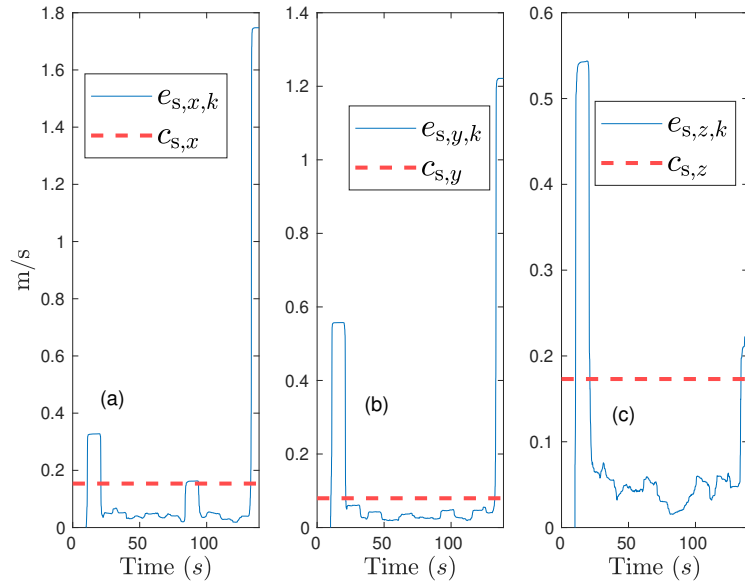


Figure 27: Example 8.1: x -axis accelerometer with bias. $e_{s,x,k}$, $e_{s,y,k}$, and $e_{s,z,k}$ remains below the cutoff threshold.

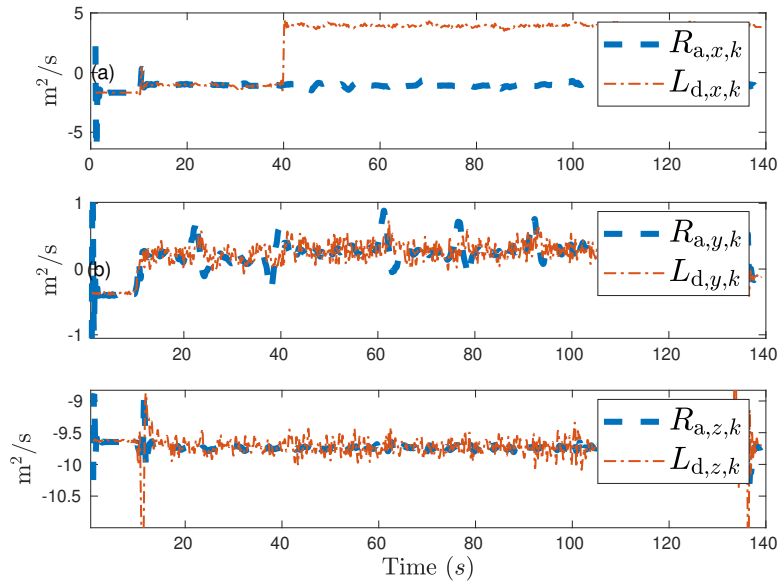


Figure 28: Example 8.1: x -axis accelerometer with bias. Beginning at 40 s, $L_{a,x,k}$ in (a) exhibit bias and thus diverge from $R_{a,x,k}$. $R_{a,y,k}$ and $R_{a,z,k}$ follows $L_{a,y,k}$ and $L_{a,z,k}$.

metrics from onboard sensor data, including radar, rate gyro, magnetometer, and accelerometer measurements, along with their derivatives. For aerial vehicles, nine kinematics-based error metrics are used to account for the additional degrees of freedom.

KSFD addresses several limitations associated with model-based and knowledge-based methods, such as the need

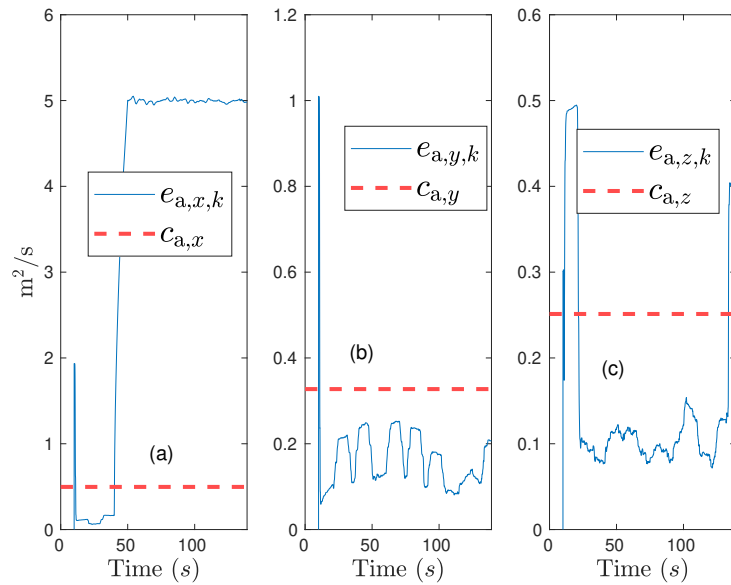


Figure 29: Example 8.1: x -axis accelerometer with bias. $e_{a,x,k}$ in (a) abruptly increases above the cutoff threshold $c_{a,x}$ at 40 s when the bias begins, which indicates that one of the sensors used to compute $e_{a,x,k}$ is faulty. $e_{a,y,k}$ and $e_{a,z,k}$ remain below the cutoff thresholds $c_{a,y}$ and $c_{a,z}$.

for accurate mathematical models and comprehensive historical data. By relying on exact kinematic relations, real-time sensor data, and AISE, KSFD reduces the complexity and computational burden typically involved in sensor-fault detection.

Simulated and experimental examples demonstrated the effectiveness of KSFD in detecting sensor faults. The results underscore the potential of KSFD for enhancing the reliability and safety of autonomous vehicles by providing robust sensor-fault-detection capabilities.

Future work will focus on refining KSFD to handle simultaneous sensor failures, expanding the applicability to a broader range of vehicles and sensor types, and integrating this technique with vehicle control systems to enable real-time, fault-tolerant operation. Finally, more advanced statistical techniques for setting the cutoff thresholds are of interest.

Acknowledgments

The authors would like to thank Juan A. Paredes for assisting with the rover and quadrotor experiment data used in this paper. This research was supported by NSF grant CMMI 2031333.

References

- [1] I. Samy, I. Postlethwaite, D.-W. Gu, Survey and Application of Sensor Fault Detection and Isolation Schemes, *Contr. Eng. Prac.* (2011).
- [2] I. Hwang, S. Kim, Y. Kim, C. E. Seah, A Survey of Fault Detection, Isolation, and Reconfiguration Methods, *IEEE Trans. Contr. Sys. Tech.* 18 (2010) 636–653.
- [3] R. Doraiswami, M. Stevenson, C. Diduch, Identification of Physical Systems: Applications to Condition Monitoring, Fault Diagnosis, Soft Sensor, and Controller Design, Wiley, 2014.
- [4] R. Isermann, Process Fault Detection Based on Modeling and Estimation Methods—A Survey, *Automatica* 20 (1984) 387–404.
- [5] R. Isermann, Supervision, Fault-Detection And Fault-Diagnosis Methods - An Introduction, *Contr. Eng. Prac.* 5 (1997) 639–652.
- [6] R. Isermann, Fault-Diagnosis Systems, Springer, 2006.
- [7] R. Isermann, Fault-Diagnosis Applications: Model-Based Condition Monitoring: Actuators, Drives, Machinery, Plants, Sensors, and Fault-tolerant Systems, Springer, 2011.

- [8] J. J. Gertler, *Fault Detection and Diagnosis in Engineering Systems*, Marcel Dekker Inc., New York, NY, 1998.
- [9] V. Venkatasubramanian, R. Rengaswamy, K. Yin, S. N. Kavuri, A Review of Process Fault Detection and Diagnosis Part I: Quantitative Model-Based Methods, *Comp. and Chem. Eng.* 27 (2003) 293–311.
- [10] R. Rengaswamy, V. Venkatasubramanian, A Fast Training Neural Network and its Updation for Incipient Fault Detection and Diagnosis, *Comp. and Chem. Eng.* 24 (2000) 431–437.
- [11] R. J. Patton, J. Chen, Observer-Based Fault Detection and Isolation: Robustness and Applications, *Contr. Eng. Prac.* 5 (1997) 671–682.
- [12] R. J. Patton, P. M. Frank, R. N. Clark, *Issues of Fault Diagnosis for Dynamic Systems*, Springer-Verlag, London, UK, 2000.
- [13] S. X. Ding, *Model-Based Fault Diagnosis Techniques: Design Schemes, Algorithms, and Tools*, Springer-Verlag, Berlin-Heidelberg, DE, 2008.
- [14] P. M. Frank, X. Ding, Survey of Robust Residual Generation and Evaluation Methods in Observer-Based Fault Detection Systems, *J. of Proc. Contr.* 7 (1997) 403–424.
- [15] L. H. Chiang, E. L. Russell, R. D. Braatz, *Fault Detection and Diagnosis in Industrial Systems*, Springer-Verlag, London, UK, 2001.
- [16] R. Rajamani, A. Ganguli, Sensor Fault Diagnostics for a Class of Non-Linear Systems Using Linear Matrix Inequalities, *Int. J. Contr.* 77 (2004) 920–930.
- [17] P. M. Frank, Fault Diagnosis in Dynamic Systems Using Analytical and Knowledge-Based Redundancy: A Survey and Some New Results, *Automatica* 26 (1990) 459–474.
- [18] E. Chow, A. S. Willsky, Analytical Redundancy and the Design of Robust Failure Detection Systems, *IEEE Trans. Autom. Contr.* 29 (1984) 603–614.
- [19] M. Staroswiecki, G. Comtet-Varga, Analytical Redundancy Relations for Fault Detection and Isolation in Algebraic Dynamic Systems, *Automatica* 37 (2001) 687–699.
- [20] J. Chen, R. J. Patton, *Robust Model-Based Fault Diagnosis for Dynamic Systems*, Springer, 2012.
- [21] X. Zhang, T. Parisini, M. M. Polycarpou, Sensor Bias Fault Isolation in a Class of Nonlinear Systems, *IEEE Trans. Autom. Contr.* 50 (2005) 370–376.
- [22] P. Freeman, P. Seiler, G. J. Balas, Air Data System Fault Modeling and Detection, *Contr. Eng. Practice* 21 (2013) 1290–1301.
- [23] K. F. Martin, A Review by Discussion of Condition Monitoring and Fault Diagnosis in Machine Tools, *Int. J. of Mach. Tools and Manuf.* 34 (1994) 527–551.
- [24] R. Kothamasu, S. H. Huang, W. H. VerDuin, System Health Monitoring and Prognostics - A Review of Current Paradigms and Practices, *Int. J. of Adv. Manuf. Tech.* 28 (2006) 1012–1024.
- [25] R. Yan, R. X. Gao, Approximate Entropy as a Diagnostic Tool for Machine Health Monitoring, *Mech. Sys. and Sig. Processing* 21 (2007) 824–839.
- [26] O. Basir, X. Yuan, Engine Fault Diagnosis Based on Multi-Sensor Information Fusion Using Dempster-Shafer Evidence Theory, *Information Fusion* 8 (2007) 379–386.
- [27] M. Basseville, Detecting Changes in Signals and Systems - A Survey, *Automatica* 24 (1988) 309–326.
- [28] M. Basseville, On-Board Component Fault Detection and Isolation Using the Statistical Local Approach, *Automatica* 34 (1998) 1391–1416.
- [29] M. Basseville, I. V. Nikiforov, *Detection of Abrupt Changes - Theory and Application*, Prentice-Hall, 1993.
- [30] G. K. Furlas, G. C. Karras, A Survey on Fault Diagnosis and Fault-Tolerant Control Methods for Unmanned Aerial Vehicles, *Machines* 9 (2021) 197.
- [31] E. Balaban, A. Saxena, P. Bansal, K. F. Goebel, S. Curran, Modeling, Detection, and Disambiguation of Sensor Faults for Aerospace Applications, *IEEE Sensors J.* 9 (2009) 1907–1917.
- [32] M. Blanke, M. Kinnaert, J. Lunze, M. Staroswiecki, *Diagnosis and Fault-tolerant Control*, 3rd Edition, 3. edition ed., Springer, 2015.
- [33] Y. Fang, H. Min, W. Wang, Z. Xu, X. Zhao, A Fault Detection and Diagnosis System for Autonomous Vehicles Based on Hybrid Approaches, *IEEE Sensors J.* 20 (2020) 9359–9371.
- [34] H. Min, Y. Fang, X. Wu, X. Lei, S. Chen, R. Teixeira, B. Zhu, X. Zhao, Z. Xu, A Fault Diagnosis Framework for Autonomous Vehicles with Sensor Self-Diagnosis, *Expert Systems with Applications* 224 (2023) 120002.
- [35] J. Cao, M. U. B. Niazi, K. H. Johansson, Sensor Fault Detection and Isolation in Autonomous Nonlinear Systems Using Neural Network-Based Observers, arXiv preprint arXiv:2304.08837, 2023.
- [36] S. Safavi, M. A. Safavi, H. Hamid, S. Fallah, Multi-Sensor Fault Detection, Identification, Isolation and Health Forecasting for Autonomous Vehicles, *Sensors* 21 (2021) 2547.
- [37] X. Han, Y. Hu, A. Xie, X. Yan, X. Wang, C. Pei, D. Zhang, Quadratic-Kalman-Filter-Based Sensor Fault Detection Approach for Unmanned Aerial Vehicles, *IEEE Sensors J.* 22 (2022) 18669–18683.
- [38] T. Huang, H. Pan, W. Sun, A Sensor Fault Detection, Isolation, and Estimation Method for Intelligent Vehicles, *Control Engineering Practice* 139 (2023) 105620.
- [39] D. Li, Y. Wang, J. Wang, C. Wang, Y. Duan, Recent Advances in Sensor Fault Diagnosis: A Review, *Sensors and Actuators A: Physical* 309 (2020) 111990.
- [40] R. C. Avram, X. Zhang, J. Campbell, J. Muse, IMU Sensor Fault Diagnosis and Estimation for Quadrotor UAVs, *IFAC-PapersOnLine* 48 (2015) 380–385.
- [41] E. Khalastchi, M. Kalech, L. Rokach, Sensor Fault Detection and Diagnosis for Autonomous Systems, in: *Proc. Int. Conf. Auton. Agents Multi-Agent Syst.*, 2013, pp. 15–22.
- [42] Y. Zhong, W. Zhang, Y. Zhang, J. Zuo, H. Zhan, Sensor Fault Detection and Diagnosis for an Unmanned Quadrotor Helicopter, *J. Intell. Robot Syst* 96 (2019) 555–572.
- [43] A. Ansari, D. S. Bernstein, Aircraft Sensor Fault Detection Using State and Input Estimation, in: *Proceedings of the American Control Conference*, Institute of Electrical and Electronics Engineers Inc., 2016, pp. 5951–5956.
- [44] A. Ansari, D. S. Bernstein, Estimation of Angular Velocity and Rate-Gyro Noise for Sensor Health Monitoring, in: *Proceedings of the American Control Conference*, 2017, pp. 128–133.
- [45] L. Van Eykeren, Q. Chu, Air Data Sensor Fault Detection Using Kinematic Relations, in: *Advances in Aerospace Guidance, Navigation and*

- Control, Springer Berlin Heidelberg, 2013, pp. 183–197.
- [46] L. Van Eykeren, Q. Chu, Sensor Fault Detection and Isolation for Aircraft Control Systems by Kinematic Relations, *Control Engineering Practice* 31 (2014) 200–210.
- [47] M. L. Fravolini, M. R. Napolitano, G. D. Core, U. Papa, Experimental interval models for the robust Fault Detection of Aircraft Air Data Sensors, *Control Engineering Practice* 78 (2018) 196–212.
- [48] R. Isermann, Model-Based Fault-Detection and Diagnosis - Status and Applications, *Annu. Rev. Control.* 29 (2004) 71–85.
- [49] S. Verma, S. Sanjeevini, E. D. Sumer, D. S. Bernstein, Real-time Numerical Differentiation of Sampled Data Using Adaptive Input and State Estimation, *International Journal of Control* (2024) 1–13.
- [50] S. Verma, B. Lai, D. S. Bernstein, Adaptive Real-Time Numerical Differentiation with Variable-Rate Forgetting and Exponential Resetting, in: *Proc. Amer. Contr. Conf.*, 2024, pp. 3103–3108.
- [51] S. Verma, S. Sanjeevini, E. D. Sumer, A. Girard, D. S. Bernstein, On the Accuracy of Numerical Differentiation Using High-Gain Observers and Adaptive Input Estimation, in: *Proc. Amer. Contr. Conf.*, 2022, pp. 4068–4073.
- [52] S. A. U. Islam, D. S. Bernstein, Recursive Least Squares for Real-Time Implementation, *IEEE Contr. Syst. Mag.* 39 (2019) 82–85.
- [53] B. Lai, D. S. Bernstein, Exponential Resetting and Cyclic Resetting Recursive Least Squares, *IEEE Contr. Sys. Lett.* 7 (2022) 985–990.
- [54] K. J. Åström, U. Borisson, et al., Theory and Applications of Self-Tuning Regulators, *Automatica* 13 (1977) 457–476.
- [55] O. Malik, G. Hope, S. Cheng, Some Issues on the Practical Use of Recursive Least Squares Identification in Self-Tuning Control, *Int. J. Contr.* 53 (1991) 1021–1033.
- [56] N. Mohseni, D. S. Bernstein, Recursive Least Squares with Variable-Rate Forgetting Based on the F-Test, in: *Proc. Amer. Contr. Conf.*, 2022, pp. 3937–3942.
- [57] J. J. McKeon, F Approximations to the Distribution of Hotelling's T_0^2 , *Biometrika* 61 (1974) 381–383.